Quantifying Bulges, Bars, and Bulgeless Galaxies Across the Hubble Sequence With Structural Decomposition

Tim Weinzirl[1], Shardha Jogee[1], & Fabio D. Barazza[2]

ABSTRACT

Structural decomposition of galaxies into bulge, disk, and bar components is important to address a number of scientific problems. Measuring bulge, disk, and bar structural parameters will set constraints on the violent and secular processes of galaxy assembly and recurrent bar formation and dissolution models. It can also help to systematically quantify the fraction and properties of bulgeless and low bulge-to-total-mass (B/T) galaxies, which defy the hierarchical LCDM paradigm of galaxy formation that requires most massive spiral galaxies to have a classical bulge. With an iterative 2D decomposition technique involving GALFIT, we perform two-component bulge-disk and three-component bulge-disk-bar decomposition on ~ 150 H-band images from the OSU Bright Spiral Galaxy Survey. The importance of including the bar component in barred galaxies is emphasized because it can cause a drastic reduction in B/T by a factor of several, as well as affect the disk component significantly. We show from the distribution of B/T and bulge Sérsic index that so-called pseudobulges (bulges with $n < 2.5$) exist in high and low-B/T systems, and in barred and unbarred systems, across the Hubble sequence, suggesting a range secular processes or mergers with low star formation efficiency may play an important role in the assembly of bulges. Bar/T, an indicator of bar strength, does not in general correlate well with Hubble type and other bar and bulge parameters (r_e, Sérsic index, stellar mass). Stellar masses are derived and we calculate the total fractional stellar mass in bulges, disks, and bars in the local Universe. It is found that 23.5% belongs to bulges (15.5% in classical bulges versus 4.7% in pseudobulges), 65.7% to disks, and 10.8% to stellar bars. We find from the cumulative fraction of galaxies as a function of B/T that $\sim 70\%$ of spiral galaxies have $B/T \leq 0.2$, in stark contrast to semi-analytic simulations of galaxy formation. We measure certain properties of low-B/T and find that, in general, galaxies with $B/T < 0.1$ are characterized by $n < 2$, disk scalelengths < 5kpc, and blue colors ($B - V < 0.7$).

[1]Department of Astronomy, University of Texas at Austin, Austin, TX

[2]Laboratoire d'Astrophysique, École Polytechnique Fédéralede Lausanne, Observatoire, Sauverny, Switzerland

1. Introduction

The formation of galaxies is a classic problem in astrophysics. Contemporary galaxy formation models combine the well-established Lambda-Cold Dark Matter (LCDM) cosmology, which describes behavior of dark matter on very large scales, with baryonic physics to model galaxy formation. In the early Universe, pockets of dark matter decoupled from the Hubble flow, collapsed into virialized halos, and then clustered hierarchically into larger structures. Meanwhile, gas aggregated in the interiors of the halos to form rotating disks, which are the building blocks of galaxies (Steinmetz & Navarro, 2002; Cole et al. 2000). Such disks are typically destroyed during mergers of their parent halos, leaving behind classical de Vaucouleurs bulges. Spiral disk galaxies formed subsequently as gaseous disks accreted around spheroids (Burkert & Naab, 2004). Only very gas-rich disks with limited star formation are able to survive mergers (Robertson et al. 2004).

Troubling inconsistencies exist between real galaxies and LCDM-based simulations of galaxy formation. One issue is the angular momentum problem; simulated galaxy disks have smaller scalelengths and, therefore, less specific angular momentum than their counterparts in nature (D'Onghia & Burkert, 2006). A second problem is the severe under prediction in the fraction of galaxies with low bulge-to-total mass ratio ($B/T < 0.2$) and of so-called bulgeless galaxies, which lack a classical bulge. Simulated spiral galaxies feature prominent classical bulges in their cores. Such predictions are in stark contradiction with emerging observations that suggest 15-20% of disk galaxies out to z $\sim$ 0.03 are bulgeless (Kautsch et al. 2006; Barazza, Jogee & Marinova, 2007)

There are many unanswered questions about the assembly of bulges, the distribution of B/T, and the properties of so-called bulgeless galaxies with low B/T. How do properties, such as disk scalelengths, mass, kinematics, colors, and star formation histories vary across galaxies of different B/T, ranging from bulge-dominated systems to quasi-bulgeless systems? Are quasi-bulgeless systems confined to low mass systems with a late onset of star formation, while classical bulges populate high mass systems that formed most of their stars at early epochs? How do the fraction, mass function, and structural properties of galaxies with different B/T vary across environments with different large-scale cosmological overdensities? If environment plays a central part in suppressing bulge formation, then differences would be expected in the properties of bulgeless galaxies in different environments, such as field versus dense galaxy clusters. How does the frequency and properties of galaxies with low B/T as a function of redshift over $z = 0.2 - 0.8$ compare to the recently reported merger history of galaxies over this epoch (Jogee et al. 2008a; Jogee et al. 2008b in prep)? Answering these questions will help us to understand the reasons behind the apparent failure of LCDM galaxy formation models, and shed light on how galaxies assemble.

Progress is possible by observationally constraining properties of enigmatic bulgeless and low B/T galaxies. A powerful and well-developed technique for measuring the structural properties (e.g. scalelengths, Sérsic indexes, B/T) of galaxies is the decomposition of the 2D light distribution into separate structural components. This is achieved by fitting an image with one or more analytic functions (e.g. Sérsic bulge, exponential disk) to make a model image. The parameters in the model are adjusted via a nonlinear least squares algorithm such that the output model matches the input image as well as possible. Naturally, the quality of the output depends on how many and what analytic functions are applied. There are several freely available implementations of 2D luminosity decomposition, including GALFIT (Peng et al. 2002), GIM2D (Simard et al. 2002), and BUDDA (de Souza et al. 2004).

Most earlier work has only performed 2D bulge-disk decomposition of unbarred galaxies. Allen et al. (2006), for example, applied GIM2D to 10,095 unbarred galaxies from the Millennium Galaxy Catalog (Liske et al. 2003; Driver et al. 2005). More recently, however, there has been a growing interest in 2D bulge-disk-bar decomposition. Laurikainen et al. (2005) has developed a 2D multicomponent decomposition code designed to model bulges, disks, primary and secondary bars, and lenses; they apply Sérsic functions to bulges and use either Sérsic or Ferrers functions to describe bars and lenses. Reese et al. (2007), have written a non-parametric algorithm to model bars in $\sim$ 70 I-band images. Also, Gadotti & Kauffman (2007) are performing 2D bulge-disk-bar and bulge-disk decomposition of 1000 barred and unbarred galaxies from SDSS with the BUDDA software.

It is important to include galactic bars in 2D decomposition. Because bars can contribute a significant fraction of a galaxy's luminosity, inclusion of the bar may be required to accurately decompose barred systems with 2D algorithms. Laurikainen et al. (2006) has shown that failure to include bars in 2D decompositions of barred galaxies yields artificially inflated bulge luminosities (Laurikainen et al. 2004). Second, late-type spirals have been shown to have higher optical bar fractions than early-type galaxies (Barazza et al. 2007). To study disk-dominated systems with little or no bulge in a meaningful way with 2D decomposition, it is therefore essential to account for the bar. Finally, bars themselves are intrinsically worth studying. Bars are present in the majority of present day spiral galaxies (Marinova & Jogee 2007 (hereafter MJ07), Eskridge et al. 2000) and provide the most important internal mechanism for redistributing angular momentum in baryonic and dark matter components (e.g., Weinberg 1985; Debattista & Sellwood 1998, 2000; Athanassoula 2002; Berentzen, Shlosman, & Jogee 2006). They efficiently drive gas inflows into the central kpc, feed central starbursts (Elmegreen 1994; Knapen et al. 1995; Hunt & Malakan 1999; Jogee et al. 1999; Jogee, Scoville, & Kenney 2005) and lead to the formation of disky, high v/σ stellar components in the inner kpc, or 'pseudobulges' (Kormendy 1993; Jogee 1999; review by Kormendy & Kennicutt 2004; Jogee, Scoville, & Kenney 2005; Athanassoula 2005).

Large-scale bars may also indirectly help to fuel AGN activity, when acting in concert with nuclear mechanisms that can reduce the specific angular momentum by several orders of magnitude. (see review by Jogee 2006 and references therein; also Mulchaey & Regan 1997; Knapen et al. 2000; Laine et al. 2002; Laurikainen et al. 2004). Finally,the prominence of strong bars out to z 1 over the last 8 Gyr (Jogee et al. 2004; Sheth et al. 2008) suggest that bars have been present over cosmological times and can impact dynamical and secular evolution of disks. Thus, quantifying bar properties can yield insight into these processes. In particular, bulge-disk-bar decomposition can provide new insights with Bar/T fractional light ratios and mass ratios.

We present 2D decompositions of 148 galaxies (86 barred and 61 unbarred). We calculate B/T, D/T, and Bar/T ratios. The decompositions are performed with an iterative method using the GALFIT code. The variation in B/T and Bar/T versus Hubble type and other bulge and bar parameters is explored. We interpret from our results implications on bulge formation scenarios. A wide range of processes, including secular evolution and mergers with low star formation efficiency, are hinted at being responsible for the construction of bulges. Stellar masses are derived, and we use them to determine the total fractional stellar mass in bulges, disks, and bars. We also explore the bulgeless galaxy problem by calculating the integrated fraction of galaxies as a function of B/T. We show that $\sim 70\%$ of spiral galaxies have $B/T \leq 0.2$, which sharply disagrees with semi-analytic simulations of galaxy formation. We also attempt to quantify certain properties of such low-B/T systems.

The plan of this paper is as follows. In §2, we describe the our data set, which consists of H-band images of bright spiral galaxies. In §3, our iterative method of 2D decomposition with GALFIT is described. In §4, tests of the integrity of our decompositions are discussed, including the generation of χ^2 ellipses. In §5, we interpret implications of our results in terms of bulges, bars, and the bulgeless galaxy problem.

2. Data

2.1. OSUBSGS

Our data set is derived from the 182 H-band images from the public data release of the Ohio State University Bright Spiral Galaxy Survey (OSUBSGS) of Eskridge et al. (2002). These galaxies are a subset of the RC3 catalog that have $M_B \leq 12$, Hubble types $0 \leq T \leq 9$, $D_{25} \leq 6'.5$, and $-80^\circ < \delta < +50^\circ$. Figure 1 shows the B-band magnitude distribution of the survey. The distribution of Hubble types peaks for intermediate (Sb-Sc) spirals (see Figure 2), and there is an deficiency of many very late types. Imaging of OSUBSGS galaxies spans

optical and infrared wavelengths with $BVRJHK$ images available for most galaxies. We choose to use the H-band images to ensure the light distribution traces stellar mass and minimizes the obscuration of the bulge by dust and star formation.

This data set has been widely used to characterize local bars and bulges, with a variety of techniques (e.g. Eskridge 2000; MJ07; Laurikainen et al. 2007) . MJ07 used the same data set to make a z $\sim$ 0 reference study for bars by applying ellipse fitting and quantitative bar selection criteria.

The OSUBSGS is a magnitude-limited survey ($M_B \leq 12$) with objects whose distances range from 3 to 56 Mpc. Faint galaxies are inevitably missed at larger distances. However, we estimate that the sample is reasonably complete for bright ($M_B < -19.3$ or $L_B = 0.33\ L^*$). The observed B-band LF is plotted against a Schechter LF (SLF) with $\Phi^* = 5.488 \times 10^{-3}$ Mpc^{-3}, $\alpha = -1.07$, and $M_B^* = -20.5$ (Efstathiou, Ellis & Peterson, 1988) in Figure 3. The volume used to determine the number density in each magnitude bin is

$$V_{max} = \frac{4\pi}{3} d_{max}^3(M) f_{sky}, \tag{1}$$

where

$$d_{max}(M) = 10^{1+0.2(m_c - M)} \tag{2}$$

and f_{sky} is the fractional sky solid angle observed (59%). d_{max} is the maximum distance out to which a galaxy of absolute magnitude M can be observed given the cutoff magnitude m_c (12 for OSUBSGS in the B-band). If the SLF is representative of the true LF, then Figure 3 suggests that the OSUBSGS sample starts to be seriously incomplete at $M_B > -19.3$, while at the brighter end (-19.3 to -23) the shape of its LF matches fairly well the SLF.

In this paper, we therefore use H-band images of the OSUBSGS sample to constrain bulge and bar properties, and address the low B/T galaxy problem for bright ($M_B < -19.3$ or $L_B = 0.33\ L^*$) massive galaxies. Our sample consists of 148 objects with $M_B < -19.3$ and inclination $i \leq 70°$.

2.2. SDSS + UKIDSS

For faint galaxies, we consider using SDSS galaxies as they have spectroscopic redshifts, stellar masses, and photometry. The stellar masses in the SDSS catalog are based on SED fits on the optical images. The SDSS spectroscopy has an r limiting magnitude of 17.7, but the image catalog systematically lacks nearby large and bright galaxies that are excluded due to limitations in the SDSS deblending software (Blanton et al. 2005). However, for faint galaxies, the SDSS sample is fairly complete. We restrict the sample to $0.001 \leq z \leq 0.01$ so

that ground-based images have adequate resolution to resolve bulges (1.2" corresponds to 246 pc at $z = 0.01$, whereas typical bulges have r_e of ∼400pc (Allen et al. 2006)).

However, in order to trace the mass distribution, NIR images are desirable over optical images. We search for an overlap between our SDSS sample and the UKIRT Infrared Deep Sky Survey (UKIDDS) (Warren et al. 2007), which is attempting to observe in the NIR many of the same fields as SDSS. We have derived a second sample from the overlap between objects in SDSS DR6 with $M_r \leq -16$ and $0.001 \leq z \leq 0.01$ and the first data release of UKDISS. Out of 1499 SDSS DR6 objects, there are 302 of matches with UKIDSS.

The luminosity functions for the SDSS and SDSS+UKIDSS samples appear in Figure 4, along with the r-band SLF. The best estimate for the volume observed in each bin is the is the volume in a spherical region with r_{min} at $z = 0.001$ and r_{max} at $z = 0.01$. Again, the volume has been corrected for the fractional sky solid angle observed by SDSS (23%). Detections in SDSS at the brightest magnitudes are nonexistent, but the sample is complete from (-16, -21.7) to within a factor of a few. Being a subset of SDSS, the SDSS+UKIDSS LF lies well below the SLF, but it has the same shape and is proportionately representative of the SDSS LF.

We plan to present to results from the decomposition of SDSS+UKIDSS galaxies in Paper II.

2.3. Stellar Masses

Stellar masses have been derived for most of the OSUBSGS sample with an empirical relation between stellar mass and rest-frame $B - V$ color. Bell et al. (2003) calculate stellar M/L ratio as a function of color using empirical functions of the form $log_{10}(M/L) = a_\lambda + b_\lambda \times Color + C$, where a_λ and b_λ are band-pass dependent constants and C is an IMF-dependent constant. In the V-band, $a_\lambda = -0.628$ and $b_\lambda = 1.305$. Assuming a Kroupa (1993) IMF, C=-0.10. Solving this expression for mass, a given $B - V$ yields a mass in $M_\odot$ of

$$M = v_{lum} 10^{-0.628+1.305(B-V)-0.10}, \tag{3}$$

where

$$v_{lum} = 10^{-0.4(V-4.82)}. \tag{4}$$

Here, V_{lum} is the luminosity parametrized in terms of absolute V magnitude. Masses were calculated in this manner for 127 (86%) objects. The remainder did not have $B - V$ colors available in RC3 or the Hyperleda database. The mass distribution is summarized in Figure 5. About 60% of the masses lie below $5 \times 10^{10} M\odot$.

As the above calculation assumes a constant M/L ratio, the mass contained within a structural component (bulge, disk, or bar) is equal to the total mass times the fractional luminosity (B/T, D/T, Bar/T) of the component. The distributions of mass in the bulge, disk, and bar versus total galaxy mass and Hubble type are shown in Figures 6 through 7. It also is possible to estimate the percentage of mass contained within each component in the local Universe: bulges (classical and pseudo bulges combined) constitute 23.5% of the available stellar mass, disks have 65.7%, and bars have 10.8%. This mass breakdown is summarized in Table 3. In §5.2.1 the breakdown in mass between classical and pseudobulges is discussed.

3. 2D Decomposition

We performed 2D, two-component bulge-disk and three-component bulge-disk-bar decomposition with GALFIT. An iterative technique that requires multiple invocations of GALFIT was developed. In this section, both the preparation needed to run GALFIT correctly and the fitting procedure itself are described.

3.1. Technique

Running GALFIT on an image requires initial preparation. The desired fitting region and sky background must be known, and the PSF image, bad pixel mask (if needed), and pixel noise map must be generated. We addressed these issues as follows:

1. Fitting region: The GALFIT fitting region must be large enough to include the entirety of the galaxy, including the outer galaxy disk. Since cutting out empty regions of sky can drastically reduce GALFIT run-time, a balance was sought between including the entire galaxy and excluding as much empty sky as possible.

2. Sky background: It is possible for GALFIT fit the sky background, but this is not recommended. When the sky is a free parameter, the wings of the bulge Sérsic profile can become inappropriately extended, resulting in a Sérsic index that is too high. Also, fitting the sky requires the fitting region to be as large as possible, increasing the run-time. For our sample, the sky background was measured separately and designated as a fixed parameter.

3. PSF: GALFIT requires a PSF image to correct for seeing effects. Statistics of many stars in each frame can be used to determine an average PSF. However, many of our

images contain only a few stars. Alternatively, a high S/N star was used as a PSF.

4. Bad pixel masks: Bad pixel masks are useful for blocking out bright stars and other image artifacts. Preparing a mask does not require the image to be explicitly altered. Our masks were ordered lists of pixel coordinates.

5. We had GALFIT internally calculate pixel noise maps for an image from the noise associated with each pixel. Noise values are determined from image header information concerning gain, read noise, exposure time, and the number of combined exposures.

GALFIT requires initial guesses for each component it fits. A Levenberg-Marquardt downhill-gradient algorithm is used to determine the minimum χ^2 based on the input guesses. GALFIT continues iterating until the χ^2 changes by less than 5e-04 for five iterations (Peng et al. 2002). In principle, it should be possible to generate reasonable guess parameters for the three-component bulge-disk-bar fit with 1D bulge-disk decomposition (this is discussed in §4.2). Instead, we elected to approach this problem with an iterative process involving three separate invocations of GALFIT. Figure 9 summarizes our method of decomposition, which we now detail.

In Stage 1, a single Sérsic component is fit to the galaxy. This serves the purpose of measuring the total luminosity, which is conserved in later stages, and the centroid of the galaxy, which is invariant in later fits. In Stage 2, the image is fit with the sum of a Sérsic bulge and an exponential disk. The output of Stage 1, (usually) being a reasonable representation of the bulge, is combined with generic input for an exponential disk. Finally, in Stage 3, a three-component model consisting of a Sérsic bulge, exponential disk, and Sérsic bar is fit. As suggested by Peng et al. (2002), the bar can be well described by an elongated, low-index Sérsic profile. For Stage 3, we provide GALFIT with input guesses for the bar parameters, along with the bulge and disk parameters output from Stage 2. The initial guesses for bar b/a and PA are based on visual inspection of the images.

In Stages 2 and 3, it is convenient to hold the disk b/a and PA constant. If these parameters are allowed to change, GALFIT may confuse the disk and bar. We set the disk parameters in concordance with the published ellipse fits ellipse fits of MJ07 as well as ellipse fits of our own.

GALFIT allows a diskiness/boxiness parameter to be added to any Sérsic and exponential profile. We did not use this parameter for any bulge or disk profiles. Bars in general have boxy isophotes, and we could have included the diskiness/boxiness parameters in the bar profiles. However, it was found that adding the parameter to the bar profile did not change the model parameters significantly, even though the appearance of the residual images improved in some cases. As accounting for bar boxiness would have only made a small

to negligible change in the derived structural parameters, we chose to neglect bar boxiness altogether.

We recognize that a drawback to any least-squares method is that a local minimum, rather than a global minimum, in χ^2 space may be converged upon. We explore this possibility with multiple tests described in §4.

3.2. Choosing the Best Fit

All objects in our sample were subjected to Stages 1, 2, and 3. Not all objects are barred, so either the Stage 2 fit or the Stage 3 fit was selected as the best. For objects with prominent bars, it was obvious that the Stage 3 model provided the best fit. More difficult are the cases with weak bars or no visual evidence for a bar. Some objects appeared to have only a bar and disk. For these objects, the Sérsic component in the Stage 2 fit matched the elongated, low-index archetype used for bars. A third bar-disk class was created for these cases. Therefore, Stage 2 can mean either a bulge-disk or a bar-disk model.

In all cases, the following criteria were applied to determine which of the Stage 2 (bulge+disk or bar+disk) or Stage 3 (bulge+disk+bar) models should be adopted.

1. GALFIT calculates a χ^2 and χ^2_ν for each model. It was found that χ^2 almost universally declined between the Stage 2 and Stage 3 fits for a given object. This is because in the Stage 3 fit, five extra free parameters (bar luminosity, r_e, Sérsic index, b/a, and PA) are added with the Sérsic bar component, allowing GALFIT to almost always make a lower χ^2 model during Stage 3. An increasing χ^2 was interpreted as a sign that the Stage 3 fit should not be adopted.

2. In cases with prominent bars, a symmetric light distribution due to unsubstracted bar light was often found in the Stage 1 and Stage 2 residuals. This was strong evidence that the Stage 3 fit be selected. NGC 4643 is shown in Figure 10 because it has a particularly striking bar residual; the corresponding fit parameters appear in Table 1. Not all barred galaxies display any such distinct or even visible residuals.

3. The Stage 2 and Stage 3 models were only selected so long as the model parameters were all well behaved. In poor fits, any of the parameters could become unphysically large or small. In galaxies with prominent bars, the bulge components of the Stage 2 fits could grow too bright and extended in size. That adding a bar in the Stage 3 fits removed this difficulty underscores the importance of accounting for the bar in

2D luminosity decomposition. Alternatively, galaxies without visual evidence for a bar could have an unphysical Stage 3 model, which favored the Stage 2 fit.

NGC 4548 is an extreme example because the Stage 2 model is bulge-dominated and has only a very faint disk. The poorness of the Stage 2 fit is attributed to the prominent bar; the combination of a Sérsic bulge and exponential disk is not adequate to describe the bulge, disk, *and* the bar. Stage 3, however,yields a believable fit with a prominent bar. The results of Stage 1, Stage 2, and Stage 3 are displayed in Figure 11 and Table 2.

4. Not all galaxies with strong bars had unphysical Stage 2 models. Instead, the bulge could be stretched along the PA of the bar, giving the bulge a lower Sérsic index and larger effective radius. A Stage 3 model that returned the bulge to a size and shape more representative of the input image was favored over the Stage 2 fit.

   Figure 12 demonstrates this behavior in NGC 4902. We distinguish this effect from cases like NGC 4548 (Figure 11) where the Stage 2 fit is completely wrong.

5. In cases where there was no bar, GALFIT was often enticed into fitting a bar to any existing spiral arms, rings, or the clumpy disks of late-type spirals. Stage 3 fits in these cases could be discarded by noting the resulting discrepancies in appearance between the galaxy images and the Stage 3 model images. Examples of false bars are shown in Figure 13.

3.3. Point Sources

For objects with bright, compact central regions, the bulge Sérsic index in the Stage 2 and Stage 3 models could grow excessively high, reaching values up to 20. Such behavior may either be caused by the presence of an AGN or a nuclear cluster. We attended to this problem by fitting a PSF as a fourth component to all objects whose initial fits had bulge Sérsic indexes > 5. A total of 48 objects required this additional PSF component. To determine how many and which of the added PSFs are due to AGN, the catalogs of Ho et al. (1997), Veron Catalog of Quasars & AGN, 12th Edition (Véron-Cetty & Véron 2006), and NED were checked. A search of the catalogs revealed 28 of these objects are classified as AGNs. Six objects are known to not be AGNs but are identified by Ho et al. (1997) as having HII nuclei. It is not clear if the remaining 14 objects have AGNs, but all appear to have bright compact sources in the nuclei. If not AGNs, the PSFs added to these objects could describe nuclear star clusters.

The fractional luminosities of the PSF components (PSF/T) are typically a few percent

or less, with several being $< 1\%$; a few are between 5-7%, and these are all confirmed AGNs. The PSF luminosity was added back to the bulge in calculating B/T. Since PSF/T is generally small, this step introduces only a small change in the final B/T of the affected galaxies. This approach was adopted as there are AGNs within the sample to which no PSF was applied. The luminosities of such AGNs are automatically included in B/T. Thus, choosing to add PSF/T and B/T where a point source was needed eliminates any systematic differences between models with and without added PSFs.

4. Self-Evaluation

To test the robustness of the fits, we performed a number of sanity checks to ensure decompositions were producing acceptable results. As stated before, the worst problem there can be with the decomposition is that the selected fits do not correspond to a global minimum in χ^2 space. A series of tests was designed to eliminate any reasonable doubt of this. These tests are now described in turn.

4.1. Simulations With Parametric Models

An obvious test is to determine if GALFIT can recover the known parameters of noise-distorted, parametric-model images. Noise-distorted models were prepared from already-existing fits produced by GALFIT. The test sample consisted of six bulge-disk-bar and four bulge-disk models with two models of each group containing extra PSF components. Gaussian noise was added to the images with PyFITS module for Python (Barrett & Bridgman, 1999). The noise was scaled by a fraction of the sky background in each image. Examples of the noisy models are shown in Figure 14.

The model images were subjected to the procedure outlined in Figure 9. GALFIT reproduced the known parameters for the barred and unbarred galaxies, including those cases with extra PSFs, to at least one decimal place in almost all cases. In addition, for the models with PSFs, very high Sérsic indexes were obtained in the Stage 2 and Stage 3 fits before extra PSF components were added to the models. That this test was successful is evidence that GALFIT is able to converge to the absolute minimum in χ^2 space for our bulge-disk and bulge-disk-bar decompositions. Ideally, GALFIT does so in all cases, but artificial simulations can only suggest this is true.

4.2. 1D Decomposition

One means of testing if GALFIT converges to a χ^2 minimum is to determine how sensitive the Stage 2 and Stage 3 fits are to the initial guesses. An alternative method of obtaining guesses for Stage 2 and Stage 3 is 1D decomposition. While 1D bulge-disk decompositions of radial profiles along the bar major axis may be influenced by the bar unless the bar region is explicitly excluded, decomposition of cuts along the bar minor axis will not be influenced as heavily. The resulting bulge and disk parameters should be adequate guesses for Stage 3 of our 2D decomposition method (Kormendy, private communication).

We test the robustness of our Stage 3 fits by extracting initial guesses for the bulge and disk using 1D decomposition along the bar minor axis. Extracting a minor-axis profile is solved using the Python PyFITS module to extract a profile along an axis specified in a DS9 region file. The resulting profiles are sky subtracted and extend out to where the intensity equals the background sky level, which is taken to be the median of all pixels in an image.

The nonlinear least-squares algorithm designed to perform the 1D decomposition simultaneously fits the sky-subtracted profiles with the sum of a Sérsic bulge and an exponential disk model. The profiles give I(r), intensity as a function of radius. The 1D algorithm fits

$$\log_{10} I(r) = \log_{10}(I_{bulge}(r) + I_{disk}(r)) \tag{5}$$

where

$$I_{bulge}(r) = 10^{a_0 + a_1 r^{a_2}} \tag{6}$$

and

$$I_{disk}(r) = 10^{a_3 + a_4 r}. \tag{7}$$

Here, a_0, a_1, a_2, a_3, and a_4 are related to the bulge and disk parameters I_e, r_e, n, I_0, and h. Initial guesses for the simultaneous bulge-disk fit are determined by independently fitting the bulge and disk over regions specified at run-time with the same nonlinear algorithm; initial guesses for these two fits are generated automatically. The results from the 1D decomposition include a bulge magnitude, r_e, Sérsic index, disk magnitude, and disk scalelength. The code to perform these decompositions was written quite easily with the aid of non-linear fitting routines from the GNU Science Library (http://www.gnu.org/software/gsl/).

The robustness of several bulge-disk-bar fits were tested by using the results of the 1D decomposition as initial guesses to Stage 3. The 1D decompositions do not provide information about the axis ratio (b/a) or PA, so these parameters for the bulge were estimated by eye; for the disk, the b/a and PA were fixed to the values determined by ellipse fitting, as described in §3.1. The initial bar parameters were unchanged from the earlier Stage 3 fits. In all cases, the new models were identical to the Stage 3 models.

4.3. χ^2 Ellipses

When running any non-linear least squares algorithm, there is the potential that the solution converged upon may represent a local minimum, rather than the absolute minimum in χ^2 space because of sensitivity on the input initial guesses. A sophisticated means of checking whether an algorithm has converged on the absolute minimum is to generate contours of the χ^2 surface. For models with N free parameters, the χ^2 space is N-dimensional. In such cases, χ^2 contours can assert whether an absolute minimum was reached by comparing two parameters at a time. If all pairs of parameters converge at the same minimum, while keeping the other parameters held to the potential best-fit parameters, then an absolute minimum has been reached.

We take such an approach with our GALFIT models. GALFIT can be made to compute χ^2 for any *pre-determined* set of parameters by instructing the software to hold all parameters fixed. We plot contoured χ^2 surfaces for every combination of magnitude, r_e (scalelength), Sérsic index, b/a, and PA for the structural components in the best fit for each galaxy. An exception was made to the disk b/a and PA, which were measured independently and held constant both here and in the original decompositions.

Calculation of the χ^2 surfaces for each parameter pair can be scripted and automated in a straightforward manner. The range explored for each parameter is determined dynamically at run-time subject to the following rules. The extent in magnitude is the model magnitude ± 1. The extent in the parameters is from 0.5-2 times the converged upon value. A cap in b/a is imposed at 1 where $2 \times b/a > 1$. In these calculations, it is important to ensure the centroid, bad pixel mask, and PSF are the same as used during the original fit. Also, for models fit with extra PSF components, provisions were made to include a PSF component whose magnitude was held fixed at all times to the converged upon value.

The surface plots are used to verify that the decompositions have reached the absolute minimum in χ^2 space for all parameters. We use contours at the $1.01 \times \chi^2$ level in each plot to determine error bars.

5. Science Discussion

In this section we consider the implications of our decompositions. Since we performed two-component bulge-disk decompositions for all objects in Stage 2, we saw firsthand the effects of adding a bar to both barred and unbarred objects. We describe some of these effects in detail and emphasize the importance of 2D bulge-disk-bar decomposition. We also discuss the implications of our results on bulge assembly and look for correlations between

bar strength and other bulge and bar parameters. Lastly, we quantify the bulgeless galaxy problem and attempt to characterize some properties of low-B/T systems.

5.1. Effect of Adding a Bar in 2D Decomposition

Including bars in 2D decomposition is extremely important. We now summarize in what ways adding bars can influence 2D decompositions of barred galaxies.

1. Modeling a bar in the Stage 3 fits forces a reshuffling of luminosity. Generally, the bulge declines in luminosity, whereas light can be either taken from, or added back, to the disk. The reshuffling of light is necessary because the Stage 2 model adjusts the bulge and disk to account for the sum of the light from the bulge, disk, *and* bar. As a result, the Stage 2 bulge in a barred galaxy can be artificially long or too bright and extended.

2. Inclusion of a bar can reduce bulge fractional luminosity B/T by a factor of two or more. Larger changes in bulge luminosities occur in cases where a prominent bar influences Stage 2 to overestimate the bulge. B/T declines in both of NGC 4643 (Figure 10 and Table 1) and NGC 4548 (Figure 11 and Table 2). In the latter case, B/T is reduced by a factor of 5 between Stage 2 and Stage 3. Such cases underscore the importance of including bars in 2D luminosity decomposition.

3. In some systems that appear dominated by a combination of a bar and disk the Stage 2 bulges are essentially bars because they match the elongated, low-index archetype Sérsic profile invoked to model bars. When a bulge could not be satisfactorily fit in Stage 3, the Stage 2 fit was retained and the object designated as a bar-disk system.

4. The scalelength of the disk is generally unchanged by including the bar. NGC 4548 is a good example. Sometimes, however, the Stage 2 disk is erroneous due to a poor fit. The Stage 3 disk parameters are quite different in such cases. NGC 4643 illustrates this behavior.

Clearly, failure to include the bar in 2D decomposition can have disastrous effects. In the most extreme cases, namely those with prominent bars, the bulge and disk could both be wrong, even with disk b/a and PA are measured independently. In more benign cases, the bulge way be stretched along the axis of the bar, and the derived B/T and D/T are still prone to be incorrect.

5.2. Bulges in the Hubble Sequence

As our sample includes galaxies from across the Hubble sequence, it is possible with this study to analyze the properties of bulges across the Hubble sequence.

The top panel in Figure 15 shows the mean and individual B/T from the bulge-disk and bulge-disk-bar decompositions plotted against Hubble type. An offset in B/T between barred from unbarred galaxies is evident by separating the two morphological types. Mean B/T declines for later types in both barred and unbarred galaxies. On the mean, barred galaxies have lower B/T than unbarred objects, yet there is much scatter and overlap in B/T exists between the two groups.

The bottom panel of Figure 15 shows variation in bulge Sérsic across the Hubble sequence. As before, barred and unbarred galaxies are distinguished, and mean values for each bin are shown. Barred galaxies have tend to have indexes < 2, though some do have higher indexes. Unbarred galaxies tend to have indexes 2, though there are some objects with lower indexes. Almost all objects have indexes < 4, indicating there are few de Vaucouleurs bulges in the sample.

Figure 16 replots bulge index against B/T. The top panel distinguishes between bar class while the bottom panel shows the distinction in Hubble type by sorting between early (S0-Sab) and late ($\geq$Sc) galaxies. The top panel indicates bars exist across a wide range in B/T and bulge index. The bottom panel suggests early-type systems have dominantly high B/T while Sc later types have lower B/T. At the same time, early types tend to have $n > 2$ while late types have $n < 2$. Again, there is some overlap between early and late types around $B/T = 0.2$.

It is evident that high-index classical bulges, which are thought to have formed in violent mergers, tend to have $B/T > 0.1$. In contrast, low-index pseudobulges ($n < 2$) exist in low and high-B/T systems throughout the Hubble sequence. The prevalence of bars in different morphologies at all Hubble types implies a range of secular processes (bars and other mechanisms too), or even mergers with low star-formation efficiencies, may contribute to the formation of pseudobulges.

5.2.1. Masses of Classical vs Pseudobulges

It is possible to estimate the percentage of mass contained in classical and pseudobulges in the local Universe. Masses were determined with the calculations described in §2.3.

Figure 8 displays bulge n versus total galaxy stellar mass. Low index ($n < 2$) systems

tend to live in low-mass systems, suggesting that pseudobulges make up a small mass fraction of the total stellar mass among all bulges. The total mass contained in bulges (classical and pseudobulges combined) constitute 23.5% of the available stellar mass. In comparison, disks have 65.7% and bars have 10.8%. Classical and pseudo bulges can be distinguished with a Sérsic index cut. The percentage of total mass in classical bulges with index > 2 is 15.5%. In comparison, the percentage of mass in pseudobulges with index < 2 is three times less at 4.7%. This suggests that although pseudobulges are found throughout the Hubble sequence, classical bulges are distinctly more massive than pseudobulges. Even if some pseudobulges exist in high-B/T systems, these must be relatively uncommon for the 3:1 mass ratio between classical and pseudobulges to hold.

5.3. Bars in the Hubble Sequence

Bulge-disk-bar decomposition allows new tests of bar strength with a measure of Bar/T luminosity fraction. Bar/T may or may not correlate with Hubble type, B/D, and bar and bulge parameters (r_e, n, and b/a). Figures 17, 18, 19, and 20 explore these possibilities and show that Bar/T does not tend correlate with well with these parameters. There is a tendency in Figure 17 for Bar/T to grow stronger with bar index. Similarly, in Figure 20 Bar/T increases as the bar grows brighter and more massive with respect to the bulge.

5.4. The Problem of Low-B/T Systems

The bulgeless galaxy problem exists because there are far too many low-B/T systems relative to what galaxy formation models imply. The standard picture of galaxy formation suggests that almost every massive galaxy should have a classical bulge. Therefore, there should be very few systems with very low B/T.

Based on our decompositions, we derive the cumulative fraction with $B/T < x$ as a function of B/T in Figure 21. In Figure 21, the curves for all galaxies, barred galaxies, and unbarred galaxies are distinguished. Both barred and unbarred galaxies show an abundance of low-B/T systems. When barred and unbarred galaxies are considered together, $\sim 70\%$ spiral galaxies have $B/T \leq 0.2$.

We compare our observational results with the simulations of the Andi Burkert group. Plotted in Figures 21 and 22 are the results for simulated galaxies that have classical bulges because they underwent at least one major merger of mass ratio 4:1 or lower. The simulations include elliptical galaxies as well as spirals, so to eliminate the ellipticals, a limiting B/T of

0.75, which is the maximum B/T determined with our decompositions, was chosen as the cutoff. The simulations are complete down to a mass of $10^8 M_\odot$. However, the mass range in our data does not extend so low. In Figure 21, a mass limit of $M \geq 4.6 \times 10^9 M_\odot$ is imposed, in line with the minimum stellar mass in our sample. In Figure 22, the mass limit is raised to $M \geq 2.5 \times 10^{10} M_\odot$. For both mass limits, the simulations severely under-predict the number of low-B/T systems. According the models, $< 10\%$ of galaxies have $B/T < 0.2$. Whereas the observed distribution of B/T begins to level off at $B/T > 0.2$, the simulated distribution increases rapidly.

The bottom panels of Figures 21 and 22 also show the fraction of B/T for different ranges of Hubble types. Curves for $3 \leq T \leq 4$ and $5 \leq T \leq 9$ contrast greatly with the simulations. In comparison, the curves for $0 \leq T \leq 2$ agree with the simulations fairly closely for $B/T < 0.3$ and $B/T < 0.4$ in Figures 21 and 22, respectively.

5.4.1. Properties of Bulgeless Galaxies

With low-B/T galaxies so much more prominent than LCDM-based simulations predict, it is important to quantify the properties of such systems and determine which region in parameter space they occupy. Relevant properties include stellar mass, bulge Sérsic index, disk scalelength, color, and specific star formation rate. We attempt to quantify these systems in a variety of ways.

The top panel of Figure 6 shows most $B/T < 0.1$ systems have stellar masses $< 5 \times 10^{10} M_\odot$. Many of these systems are barred. However, there are barred and unbarred systems with low B/T that have higher stellar masses, and some low stellar mass systems have $B/T > 0.1$. If a total stellar mass of $5 \times 10^{10} M_\odot$ is taken to be an approximate upper bound for low-B/T systems, then Figure 8, which plots bulge Sérsic index as a function of stellar mass, indicates many low-B/T systems have $n < 2$.

The top panel of Figure 23 plots $B-V$ color against bulge index. There is a large amount of scatter, but the objects with the lowest bulge indexes have the bluest colors. Systems with the highest bulge indexes have the the reddest colors. The bottom panel of Figure 23 plots $B-V$ against B/T. It is evident that galaxies with $B/T < 0.1$ have $B-V < 0.7$ and are bluer overall compared to galaxies with the most massive bulges.

The top and bottom panels of Figure 24 plot the distribution of disk scalelength against bulge index and B/T, respectively. From the top panel, galaxies with $n < 2$ tend to have scalelengths < 5kpc; for $n > 2$, scalelengths are generally > 2kpc. From the bottom panel, systems with $B/T < 0.1$ have scalelengths < 5kpc.

Figure 25 plots $B-V$ against disk scalelength. The top panel is coded according to bulge index, while the bottom panel differentiates between B/T. The top panel indicates galaxies with $n < 2$ dominantly have $B-V < 0.7$ and disk scalelength $<$ 5kpc. The bottom panel indicates galaxies with $B/T < 0.1$ tend to have $B-V < 0.7$ and disk scalelength $<$ 5kpc. Thus, low-B/T systems are found to in general have pseudobulges ($n < 2$), disk scalelengths $<$ 5kpc, and blue colors ($B-V < 0.7$).

6. Summary

Structural decomposition of galaxy light distributions is relevant to a number problems. Although most previous 2D decompositions have focused on two-component bulge-disk decomposition, including bars in 2D decomposition is crucial because it is required to accurately model the bulge and disk in barred galaxies. As most spiral galaxies (especially late-type systems) are barred, a sound method of bulge-disk-bar decomposition is required to constrain galaxy formation models and quantify the bulgeless galaxy problem with structural decomposition. Therefore, in this paper we have developed an iterative 2D, bulge-disk-bar decomposition technique using GALFIT. H-band images of bright, massive spiral galaxies from OSUBSGS are fit with parametric models that are the sum of Sérsic and exponential profiles. Bars are fit with a low-index, elongated Sérsic profile, while a Sérsic and exponential profile are used for the bulge and disk.

Our main results are the following.

1. The importance of including the bar component in 2D structural decomposition of barred galaxies is emphasized because it can cause a drastic reduction in B/T by a factor of several, as well as affect the disk component significantly. Examples of the affect of including the bar are provided for the prominently barred galaxies NGC 4643 (Figure 10, Table 1) and NGC 4548 (Figure 11, Table 2).

2. From the distribution of B/T and bulge Sérsic index (Figures 15 and 16) pseudobulges are found to exist in high and low-B/T systems, and in barred and unbarred systems, across the Hubble sequence. This suggests a range secular processes, including bars and mergers with low star formation efficiency, may play an important role in the assembly of bulges.

3. Modeling bars with 2D decomposition also allows quantitative measure of bar properties (r_e, n, b/a) and bar strength Bar/T. Bar strength, does not in general correlate well with stellar mass, Hubble type, and bulge and bar parameters like r_e, Sérsic index (see Figures 6-7,17-20).

4. Stellar masses are derived from $B-V$ colors. Assuming a constant M/L ratio, we use the B/T, D/T, and Bar/T luminosities ratios from our decompositions to calculate the fractional stellar mass in bulges, disks, and bars in the local Universe. It is found that 23.5% of stellar mass belongs to bulges (15.5% in classical bulges versus 4.7% in pseudobulges), 65.7% to disks, and 10.8% to stellar bars.

5. We find from the cumulative fraction of galaxies as a function of B/T that $\sim 70\%$ of spiral galaxies have $B/T \leq 0.2$, in stark contrast to semi-analytic simulations of galaxy formation (see Figures 21 and 22)

6. We attempt to quantify certain properties of low-B/T systems. It is found from Figures (6, 8, 23, 24, and 25) that galaxies with $B/T < 0.1$ have, in general, $n < 2$, disk scalelengths < 5kpc, and blue colors ($B - V < 0.7$).

REFERENCES

Allen, P. D., Driver, S. P., Graham, A. W., Cameron, E., Liske, J., & de Propris, R. 2006, MNRAS, 371, 2

Athanassoula, E. 2002, ApJ, 569, L83

Athanassoula, E. 2005, MNRAS, 358, 1477

Barazza, F. D., Jogee, S., & Marinova, I. 2007, IAU Symposium, 235, 76

Barrett, P. E., & Bridgman, W. T. 1999, Astronomical Data Analysis Software and Systems VIII, 172, 483

Bell, E. F., McIntosh, D. H., Katz, N., & Weinberg, M. D. 2003, ApJS, 149, 289

Berentzen, I., Shlosman, I., & Jogee, S. 2006, ApJ, 637, 582

Blanton, M. R., Lupton, R. H., Schlegel, D. J., Strauss, M. A., Brinkmann, J., Fukugita, M., & Loveday, J. 2005, ApJ, 631, 208

Burkert, A., & Naab, T. 2004, Coevolution of Black Holes and Galaxies, 421

Cole, S., Lacey, C. G., Baugh, C. M., & Frenk, C. S. 2000, MNRAS, 319, 168

Debattista, V. P., & Sellwood, J. A. 1998, ApJ, 493, L5

de Souza, R. E., Gadotti, D. A., & dos Anjos, S. 2004, ApJS, 153, 411

D'Onghia, E., Burkert, A., Murante, G., & Khochfar, S. 2006, MNRAS, 372, 1525

Driver, S. P., Liske, J., Cross, N. J. G., De Propris, R., & Allen, P. D. 2005, MNRAS, 360, 81

Efstathiou, G., Ellis, R. S., & Peterson, B. A. 1988, MNRAS, 232, 431

Elmegreen, B. G. 1994, ApJ, 425, L73

Eskridge, P. B., et al. 2000, AJ, 119, 536

Eskridge, P. B., et al. 2002, ApJS, 143, 73

Gadotti, D., & Kauffmann, G. 2007, IAU Symposium, 241, 507

Ho, L. C., Filippenko, A. V., & Sargent, W. L. W. 1997, ApJS, 112, 315

Hunt, L. K., & Malkan, M. A. 1999, ApJ, 516, 660

Jogee, S. 1999, Ph.D. Thesis,

Jogee, S., Kenney, J. D. P., & Smith, B. J. 1999, ApJ, 526, 665

Jogee, S., et al. 2004, ApJ, 615, L105

Jogee, S., Scoville, N., & Kenney, J. D. P. 2005, ApJ, 630, 837

Jogee, S. 2006, Physics of Active Galactic Nuclei at all Scales, 693, 143

Jogee, S., et al. 2008, ArXiv e-prints, 802, arXiv:0802.3901

Kautsch, S. J., Grebel, E. K., Barazza, F. D., & Gallagher, J. S., III 2006, A&A, 445, 765

Knapen, J. H., Beckman, J. E., Heller, C. H., Shlosman, I., & de Jong, R. S. 1995, ApJ, 454, 623

Knapen, J. H., Shlosman, I., & Peletier, R. F. 2000, ApJ, 529, 93

Kormendy, J. 1993, Galactic Bulges, 153, 209

Kormendy, J., & Kennicutt, R. C., Jr. 2004, ARA&A, 42, 603

Kroupa, P., Tout, C. A., & Gilmore, G. 1993, MNRAS, 262, 545

Laine, S., Shlosman, I., Knapen, J. H., & Peletier, R. F. 2002, ApJ, 567, 97

Laurikainen, E., Salo, H., Buta, R., & Vasylyev, S. 2004, MNRAS, 355, 1251

Laurikainen, E., Salo, H., & Buta, R. 2005, MNRAS, 362, 1319

Laurikainen, E., Salo, H., Buta, R., Knapen, J., Speltincx, T.,

Laurikainen, E., Salo, H., Buta, R., & Knapen, J. H. 2007, MNRAS, 381, 401 & Block, D. 2006, AJ, 132, 2634

Liske, J., Lemon, D. J., Driver, S. P., Cross, N. J. G., & Couch, W. J. 2003, MNRAS, 344, 307

Marinova, I., & Jogee, S. 2007, ApJ, 659, 1176

Mulchaey, J. S., & Regan, M. W. 1997, ApJ, 482, L135

Paturel G., Petit C., Prugniel P., Theureau G., Rousseau J., Brouty M., Dubois P., Cambrésy L., 2003, A&A, 412, 45

Peng, C. Y., Ho, L. C., Impey, C. D., & Rix, H.-W. 2002, AJ, 124, 266

Reese, A. S., Williams, T. B., Sellwood, J. A., Barnes, E. I., & Powell, B. A. 2007, AJ, 133, 2846

Robertson, B., Yoshida, N., Springel, V., & Hernquist, L. 2004, ApJ, 606, 32

Sheth, K., et al. 2008, ApJ, 675, 1141

Simard, L., et al. 2002, ApJS, 142, 1

Steinmetz, M., & Navarro, J. F. 2002, New Astronomy, 7, 155

Véron-Cetty, M.-P., & Véron, P. 2006, A&A, 455, 773

Warren, S. J., et al. 2007, MNRAS, 375, 213

Weinberg, M. D. 1985, MNRAS, 213, 451

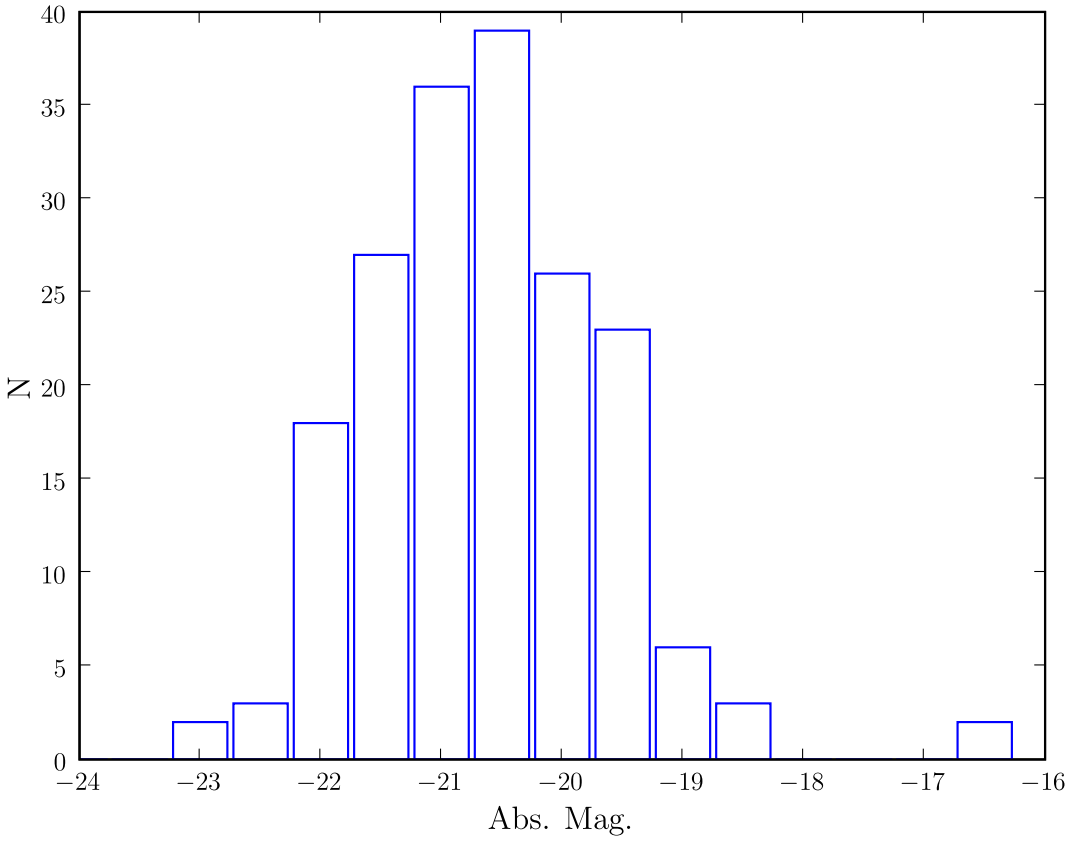

Fig. 1.— The distribution of B-band magnitudes for OSUBSGS. The magnitudes are taken from the Hyperleda (Paturel et al. 2003) database.

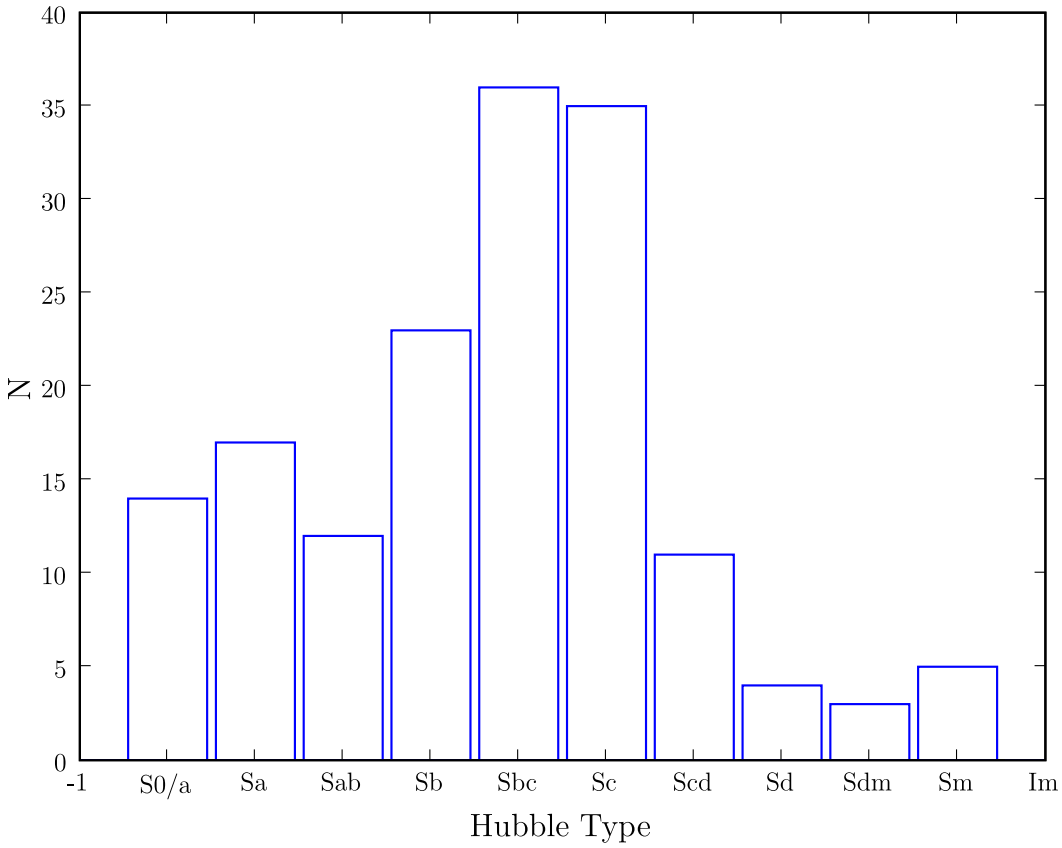

Fig. 2.— The distribution of Hubble types for OSUBSGS. The peak in the distribution occurs at Sb-Sbc. There is clearly a deficiency in late-types.

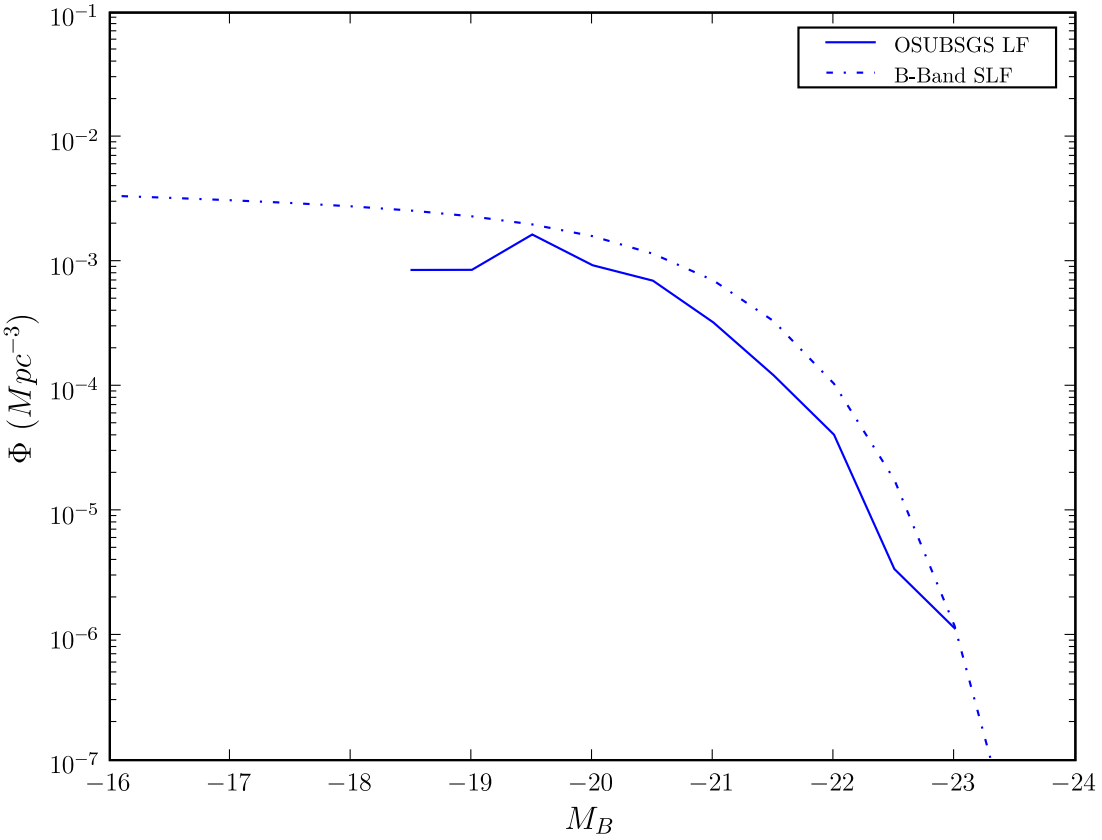

Fig. 3.— The OSUBSGS luminosity function is compared the B-band Schechter luminosity function (SLF). The former is calculated as described in §2.1 using equation (1). The parameters for the SLF are $\Phi^* = 5.488 \times 10^{-3}$ Mpc^{-3}, $\alpha = -1.07$, and $M_B^* = -20.5$, corresponding to H_0=70 km/s Mpc^{-1}.

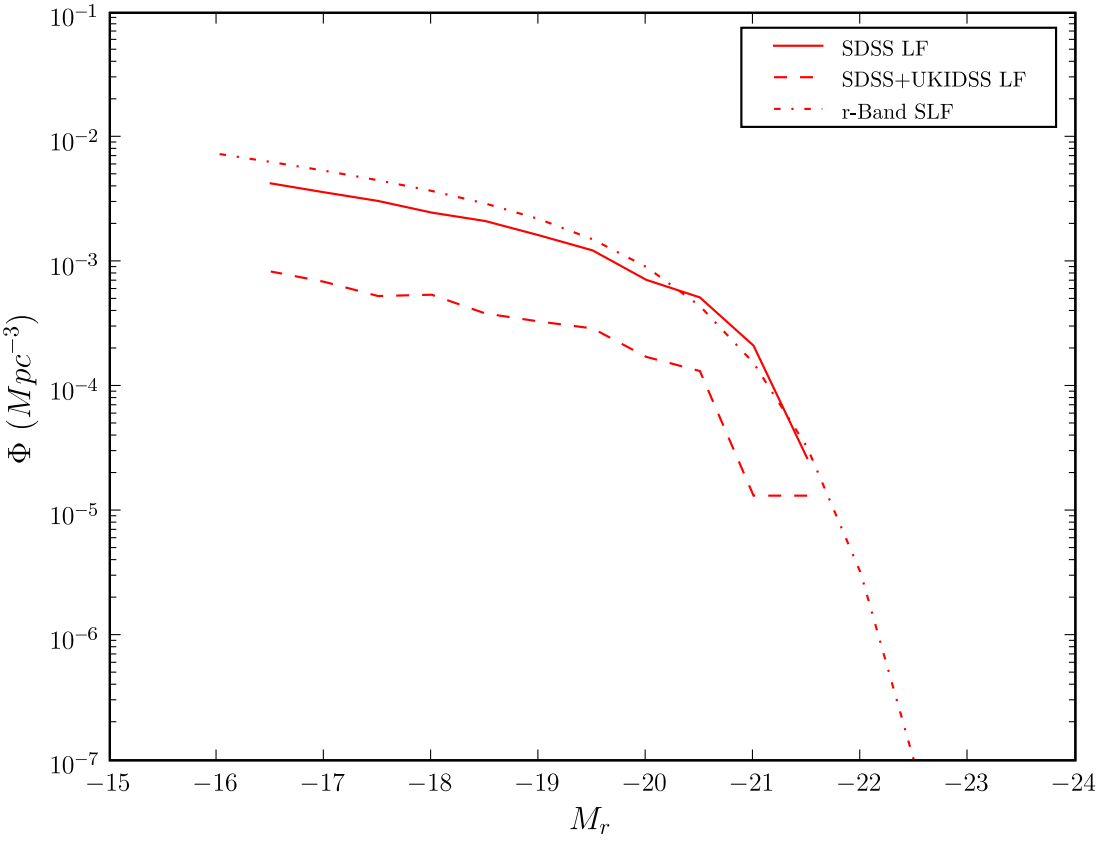

Fig. 4.— The r-band SDSS and SDSS+UKIDSS luminosity functions are compared to the r-band Schechter luminosity function (SLF). Though the SDSS+UKDISS curve is several orders of magnitude less than the curve for the full SDSS sample, it still has the same shape as the SLF. The parameters adopted for the SLF are (following Blanton et al. (2005)) $\Phi^* = 5.488 \times 10^{-3}$ Mpc^{-3}, $\alpha = -1.3$, and $M_r^* = -19.7$, corresponding to to H_0=70 km/s Mpc^{-1}. The volume considered in each bin is the co-moving volume enclosed between redshifts 0.001 and 0.01, multiplied by the fraction of sky observed surveyed by SDSS (23%).

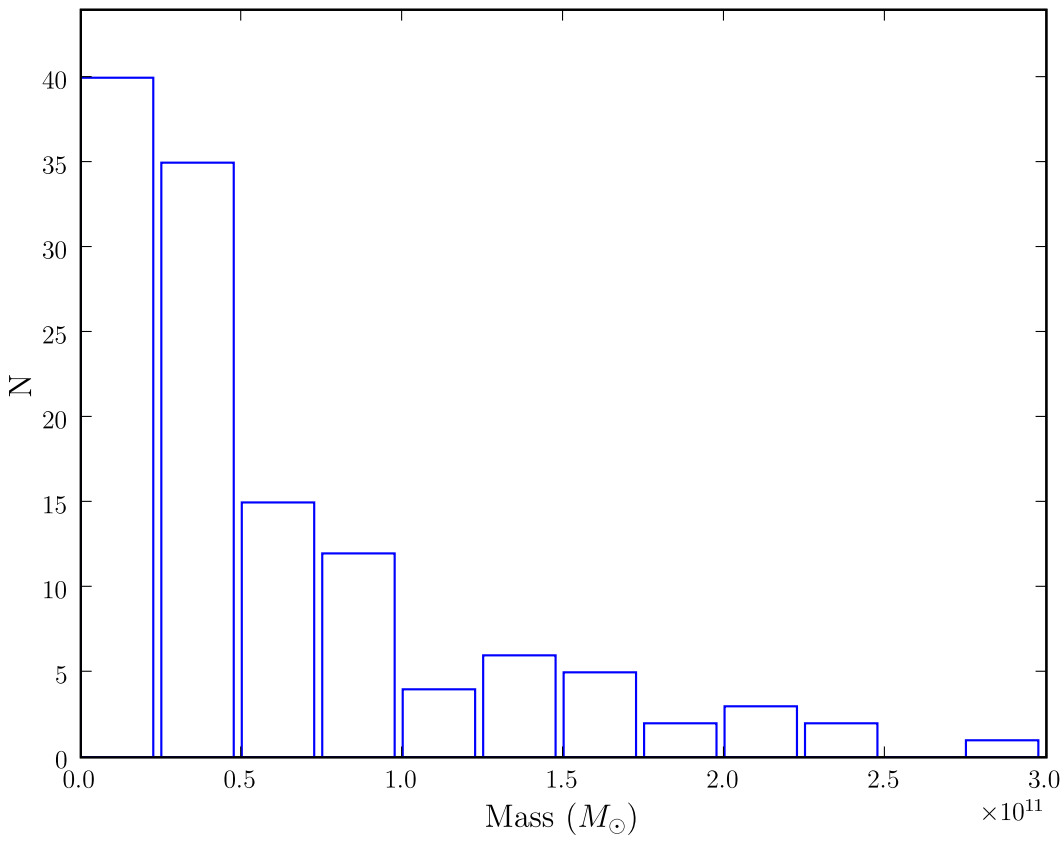

Fig. 5.— Mass distribution of OSUBSGS galaxies as determined in §2.3 using $B-V$ colors.

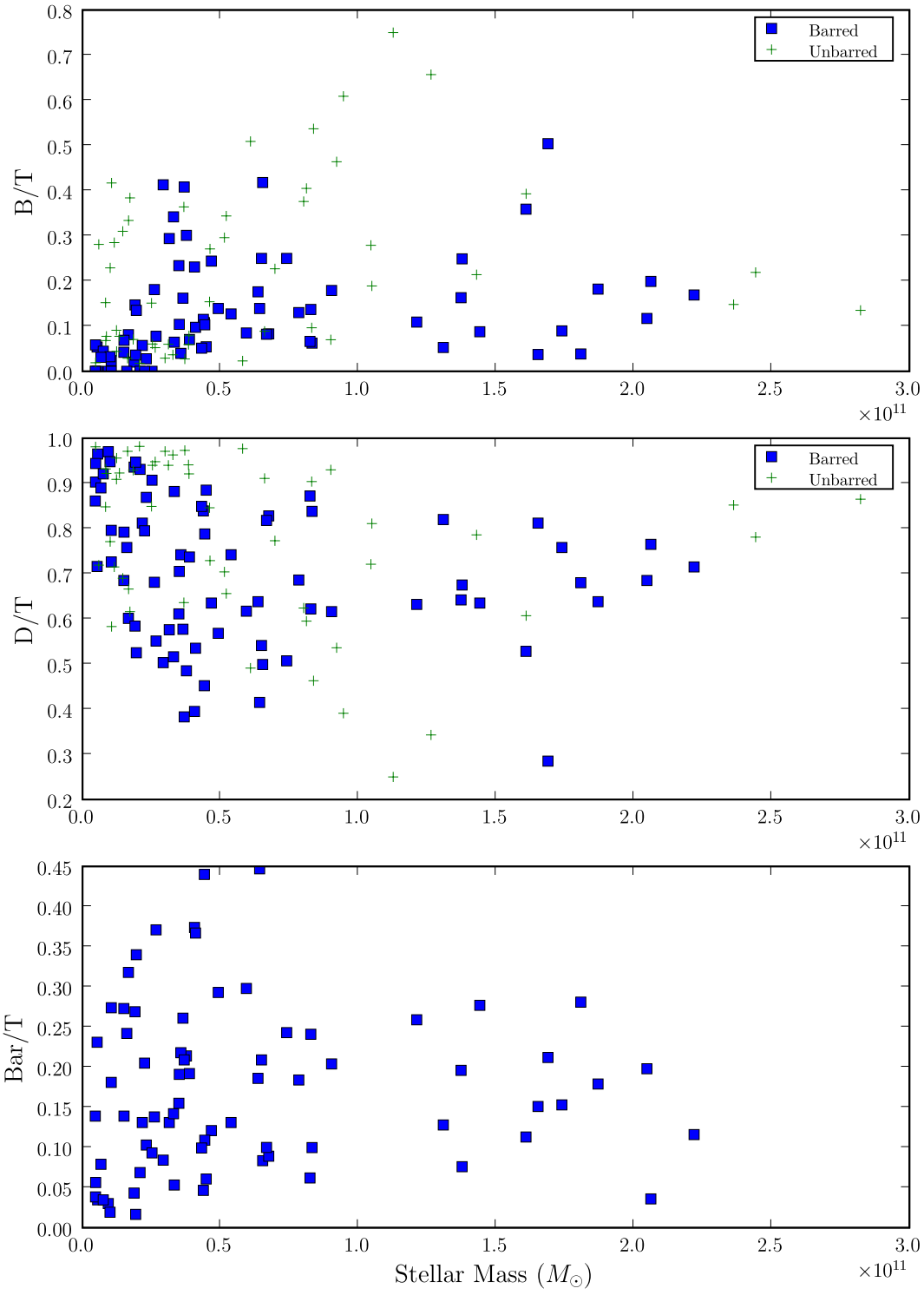

Fig. 6.— The top, middle, and bottom panels show distributions of B/T, D/T, and Bar/T, respectively, as functions of stellar mass. In the top panel, the B/T of barred and unbarred galaxies are mixed at all stellar masses. In the middle panel, galaxies with $D/T \sim 1$ tend to be low-mass systems, whereas higher mass systems have a wider range of D/T. In the bottom panel, a range of Bar/T exist at all masses.

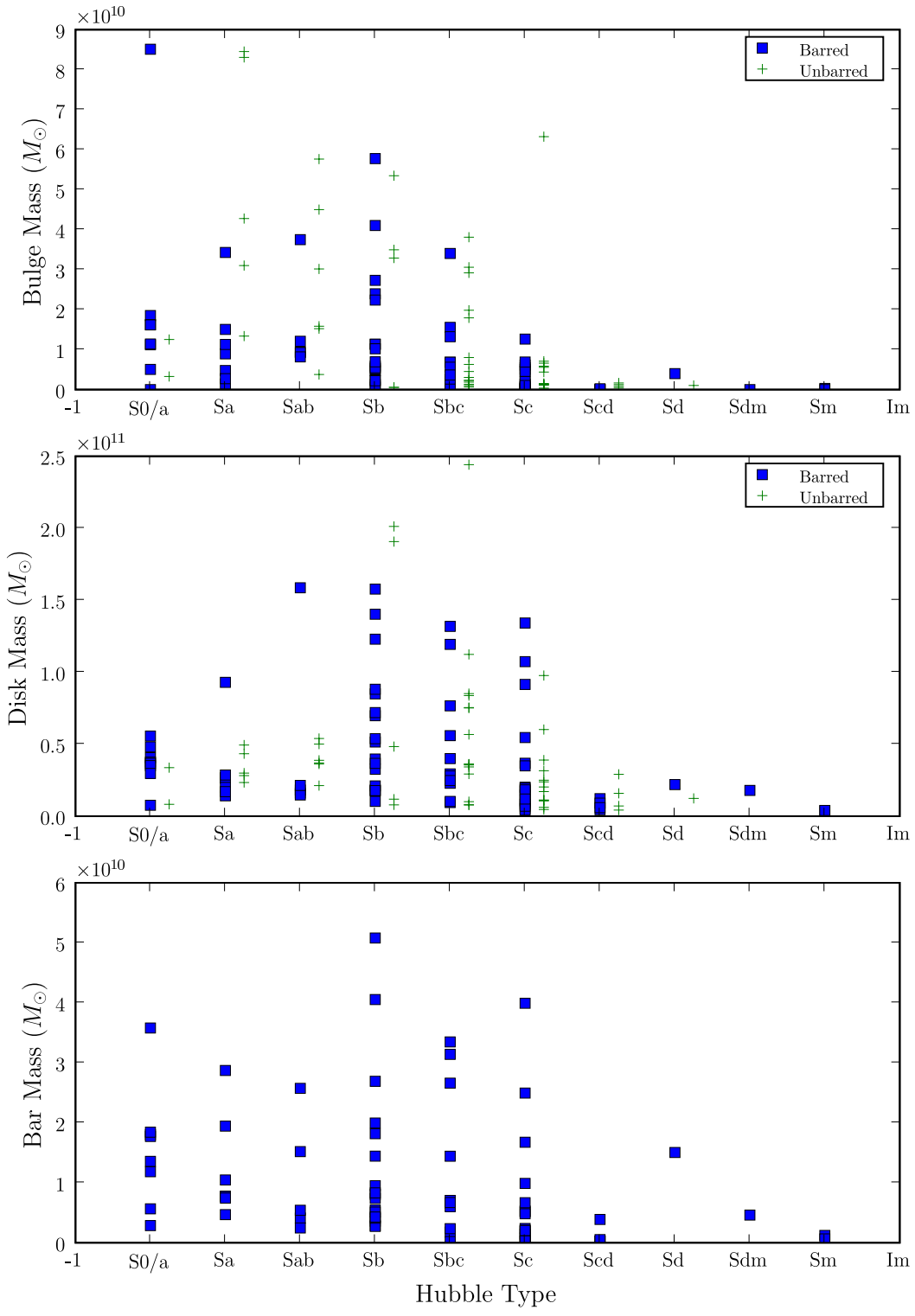

Fig. 7.— The top, middle, and bottom panels show stellar mass for bulges, disks, and bars, respectively, along the Hubble sequence. Late types ($T \geq Scd$) tend to have the smallest stellar mass components.

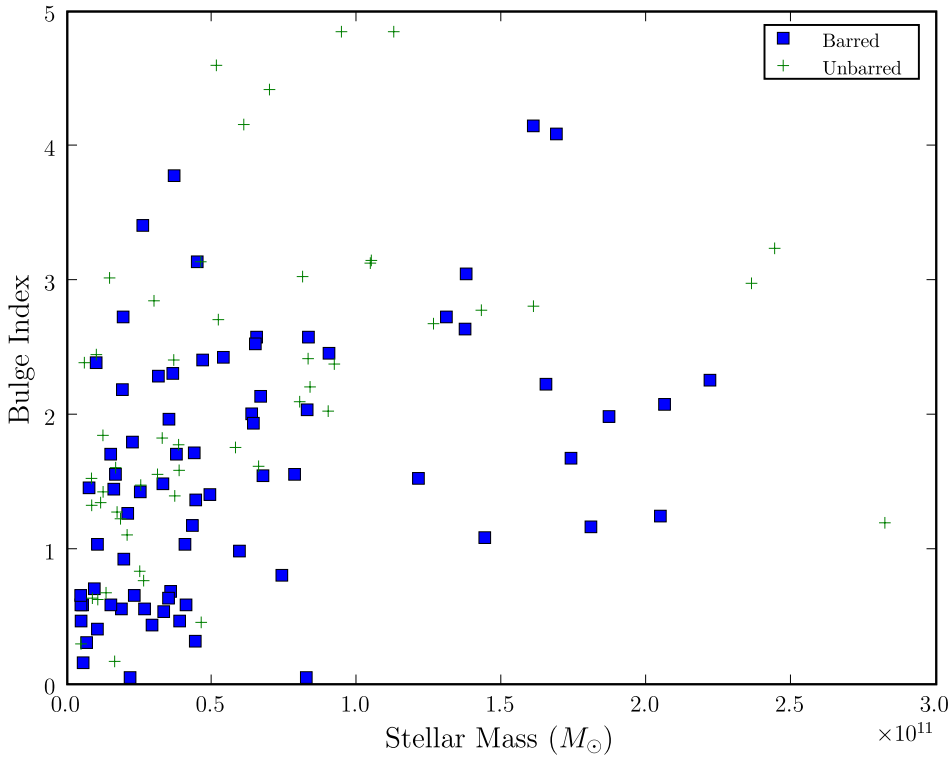

Fig. 8.— Bulge Sérsic index is plotted against galaxy stellar mass. Low-index ($n < 2.5$) systems tend to have stellar masses inside $M \leq 10^{10} M_\odot$. Higher-index systems have a wide range of stellar mass.

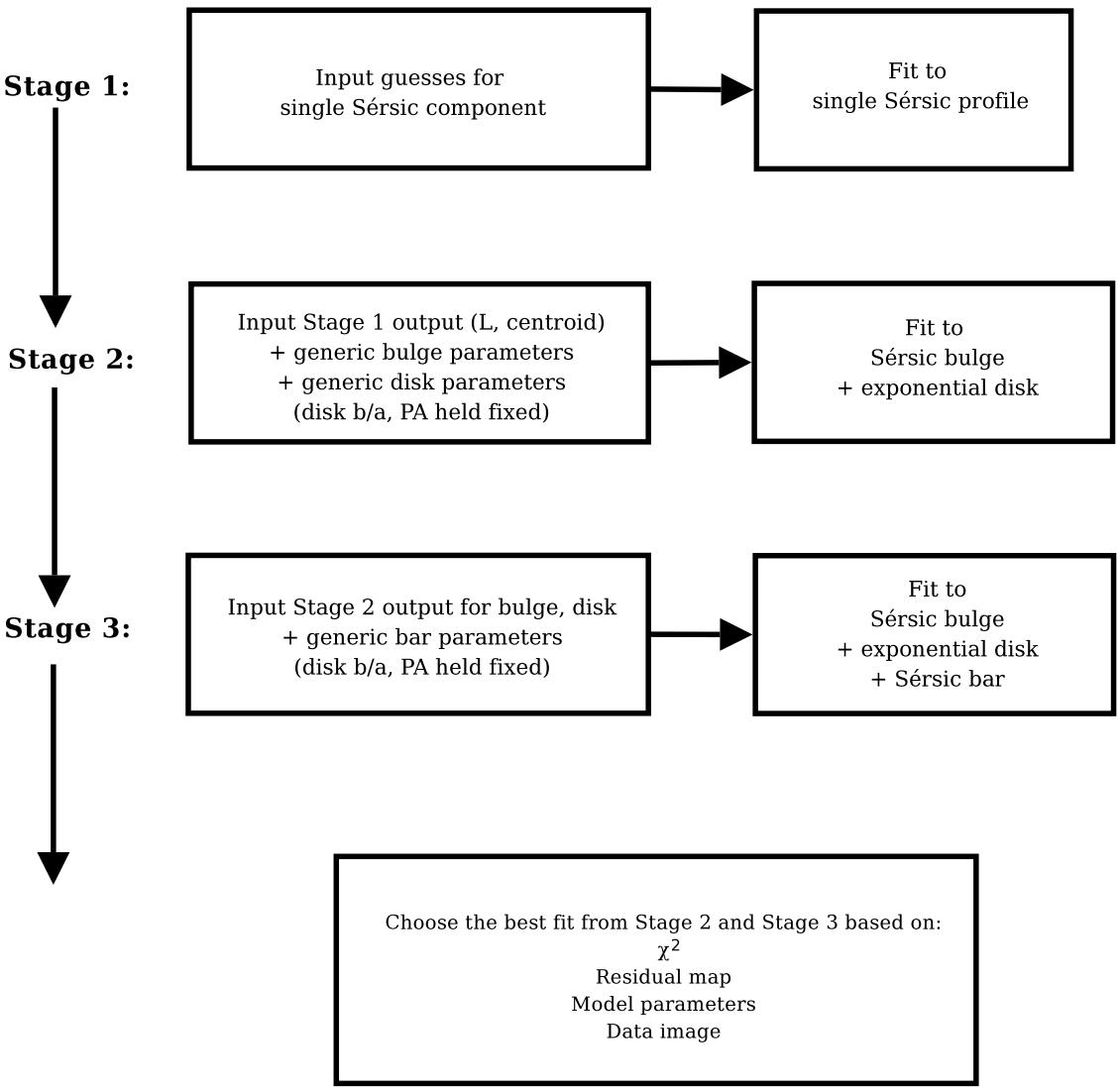

Fig. 9.— Overview of fitting procedure.

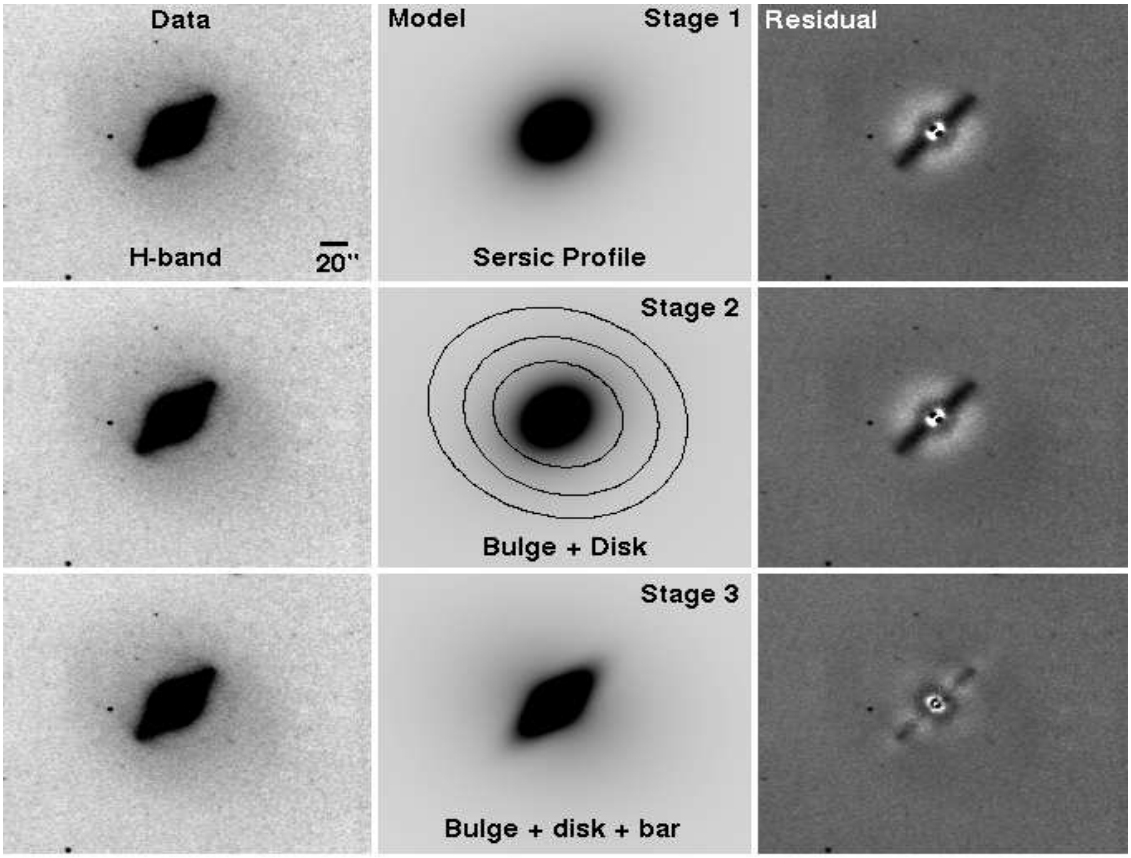

Fig. 10.— Complete decomposition for NGC 4643. Note the prominent bar residuals in the Stage 1 and Stage 2 residuals. This is a case where the prominent bar causes the Stage 2 fit to artificially extend the bulge and inflate the B/T. The disk in Stage 2 is fit with a very dim and extended structure not visible in the image. Contours show the disk b/a and PA. See Table 1 for the fit parameters.

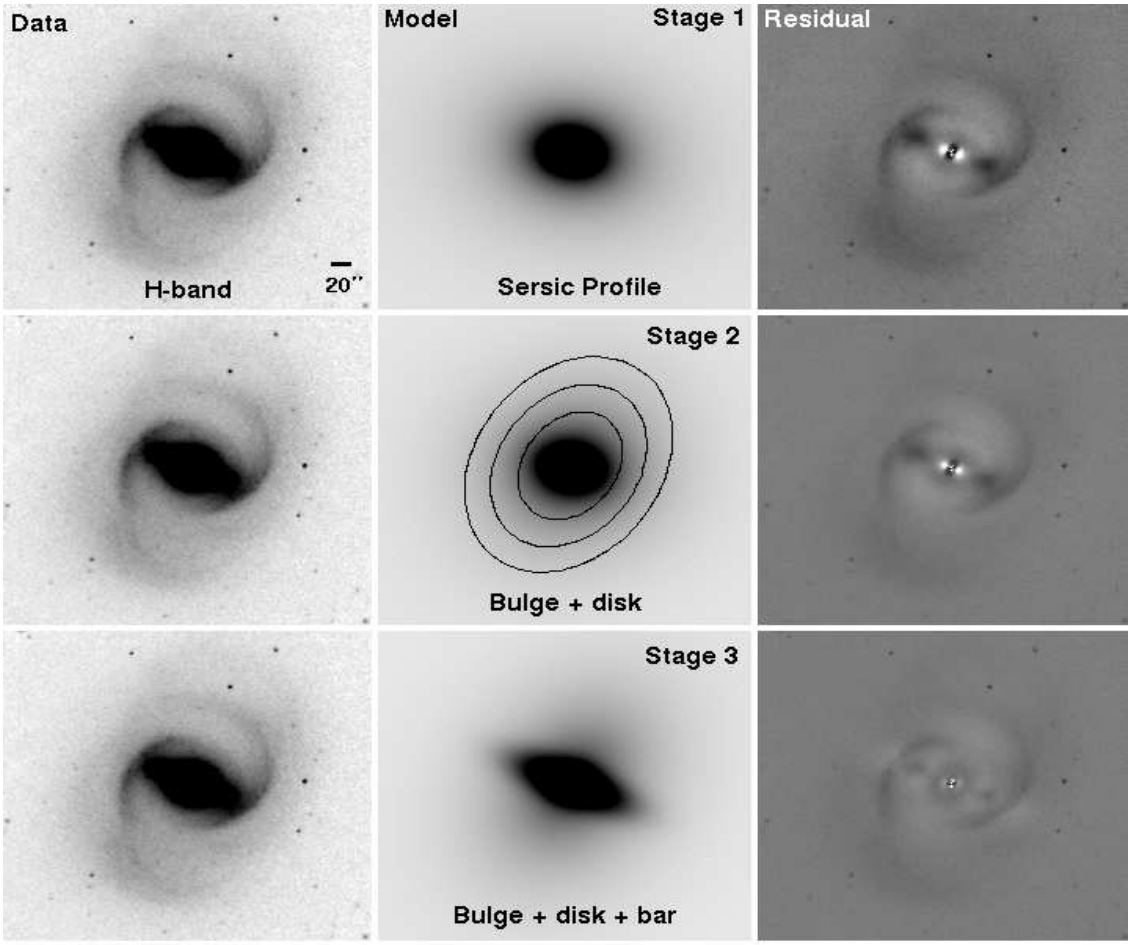

Fig. 11.— The complete decomposition for NGC 4548. This is an extreme example where the prominent bar results in an extended bulge and inflated B/T in the Stage 2 fit. Like NGC 4643 in Figure 10, the disk component is too faint to be visible. Contours show the disk b/a and PA. See Table 2 for the fit parameters.

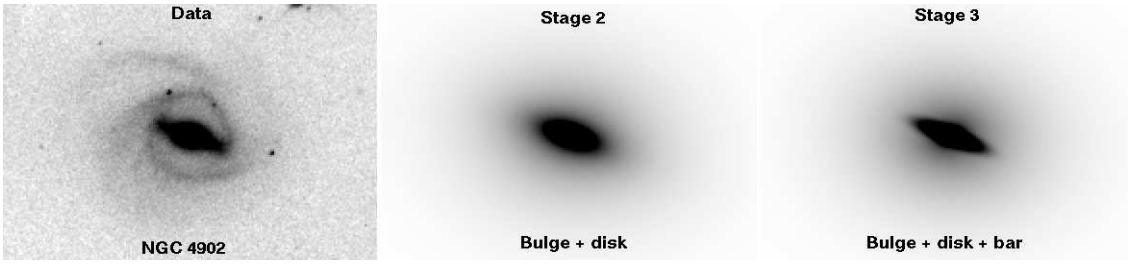

Fig. 12.— This plot shows the data image, Stage 2 model, and Stage 3 model for NGC 4902. The Stage 2 bulge is too bright and extended along the major axis of the bar (B/T=31.2% and b/a=0.45). In Stage 3, the bulge and bar are fit with distinct components (B/T=6.2%, bulge b/a=0.75, Bar/T=10.0%, bar b/a=0.25).

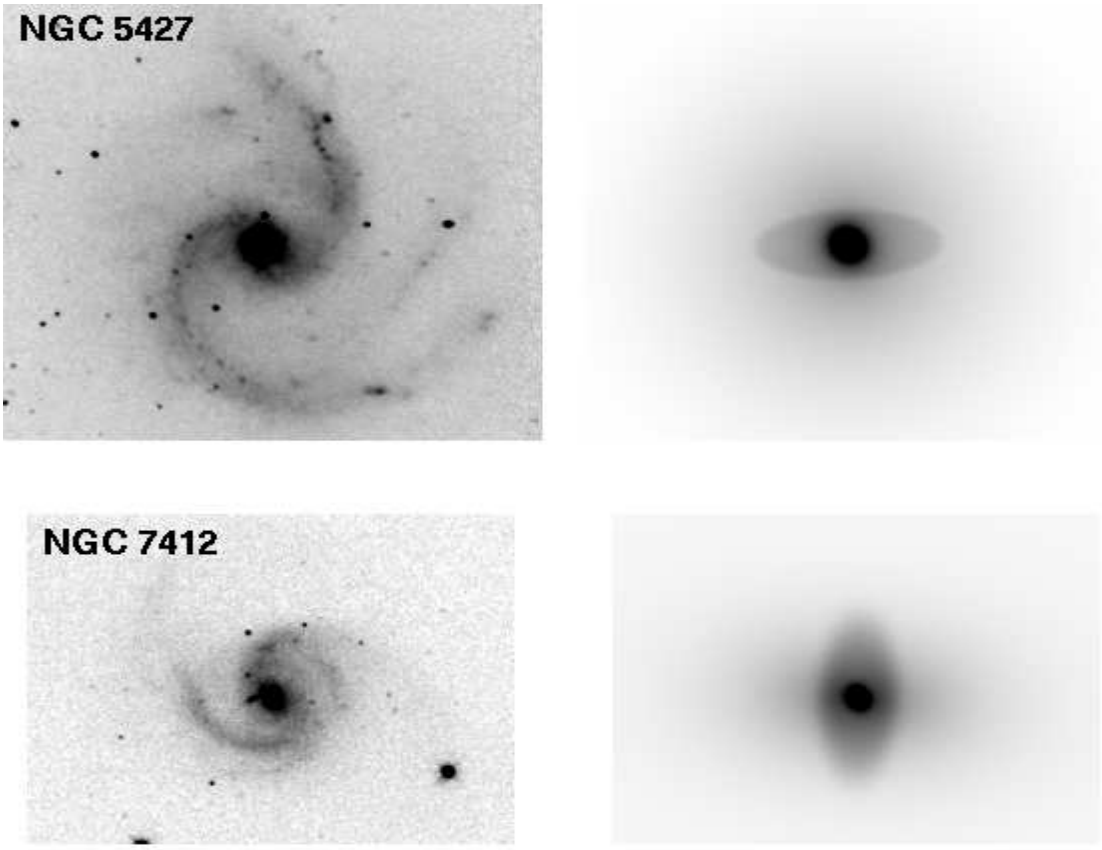

Fig. 13.— The data images and Stage 3 models of NGC 5427 and NGC 7412 are shown. The Stage 3 models each distinctly show a bar component not present in the data images, making the bar components false.

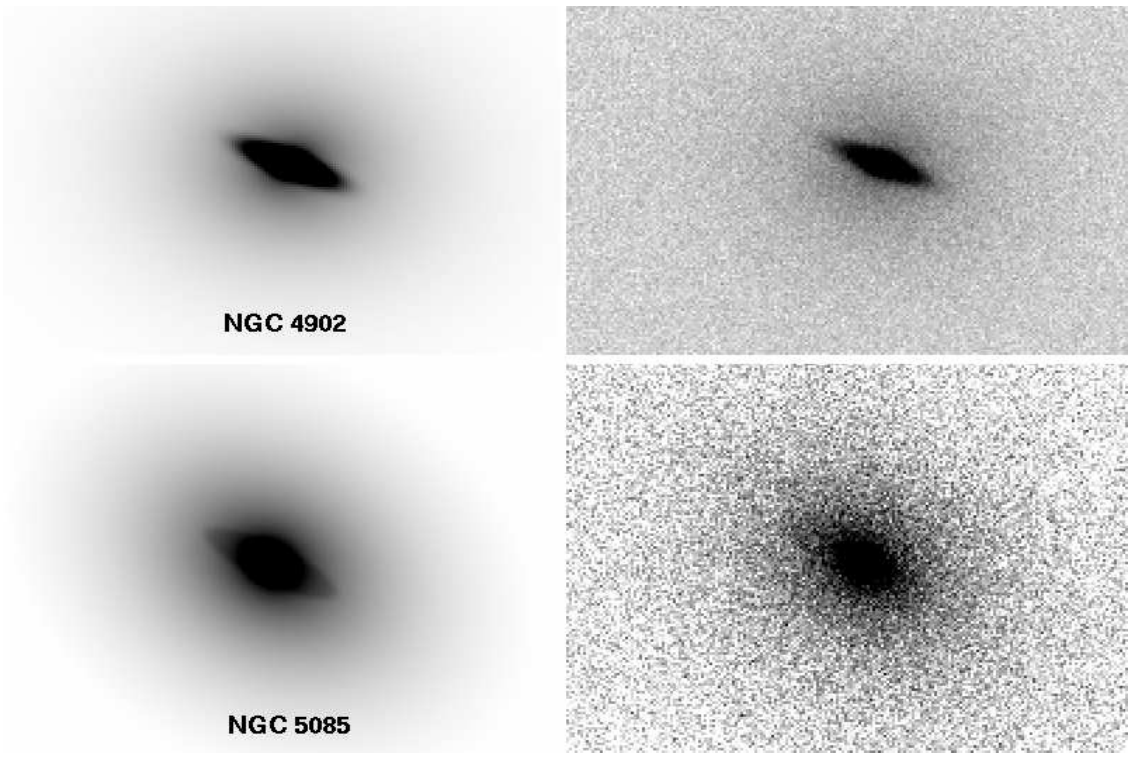

Fig. 14.— Original and distorted models from the simulations described in §4.1. The upper panels are the original and noise-distorted models for NGC 4902. The bottom panels apply to NGC 5085. The distorted model for NGC 5085 is relatively more noisy.

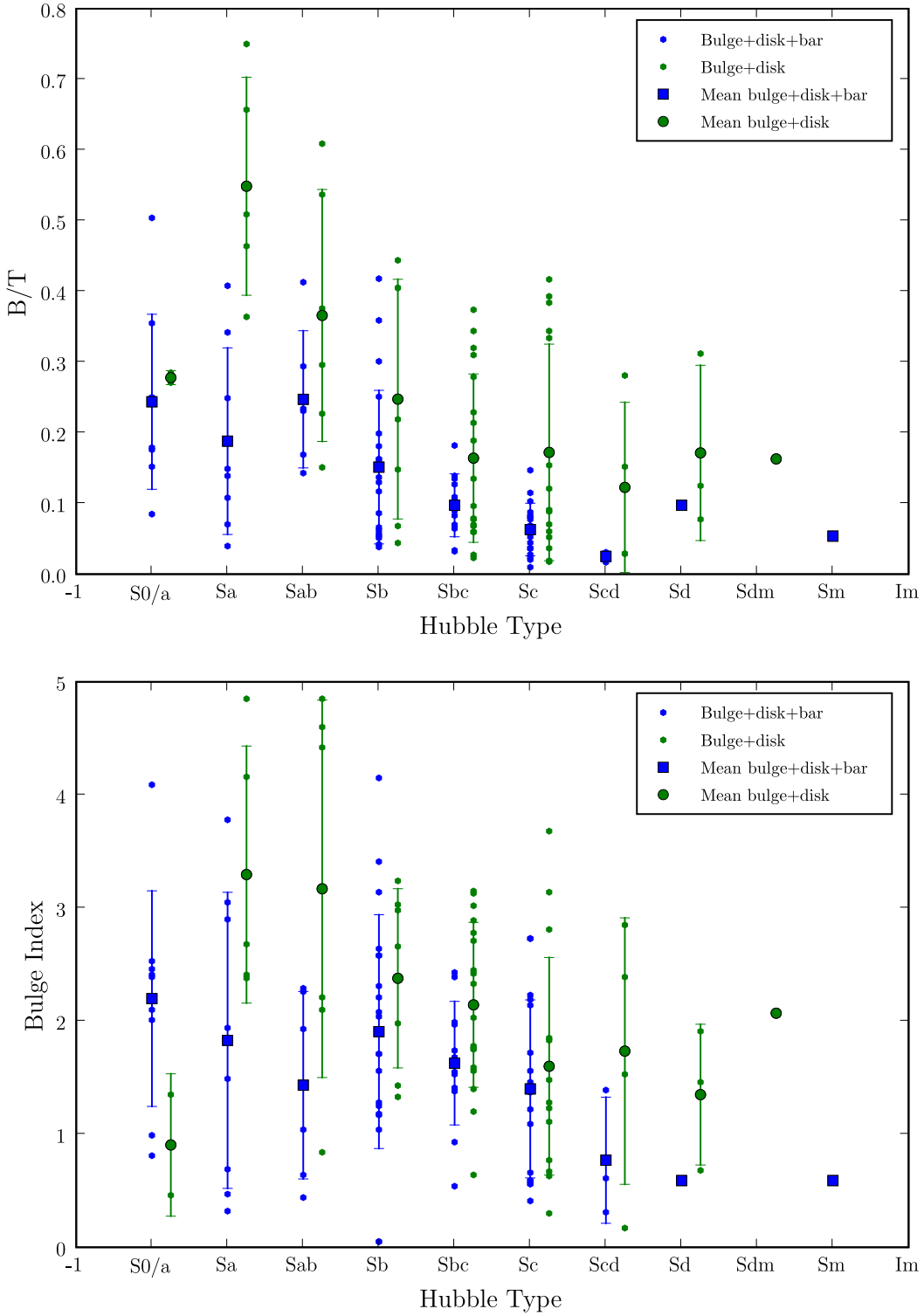

Fig. 15.— The individual and mean B/T and bulge Sérsic indexes are plotted along the Hubble sequence. Bulges in barred galaxies differ systematically on the mean from unbarred galaxies, though there is much overlap in parameter space between barred and unbarred systems. The bottom panel shows low-index ($n < 2.5$) exist throughout the Hubble sequence.

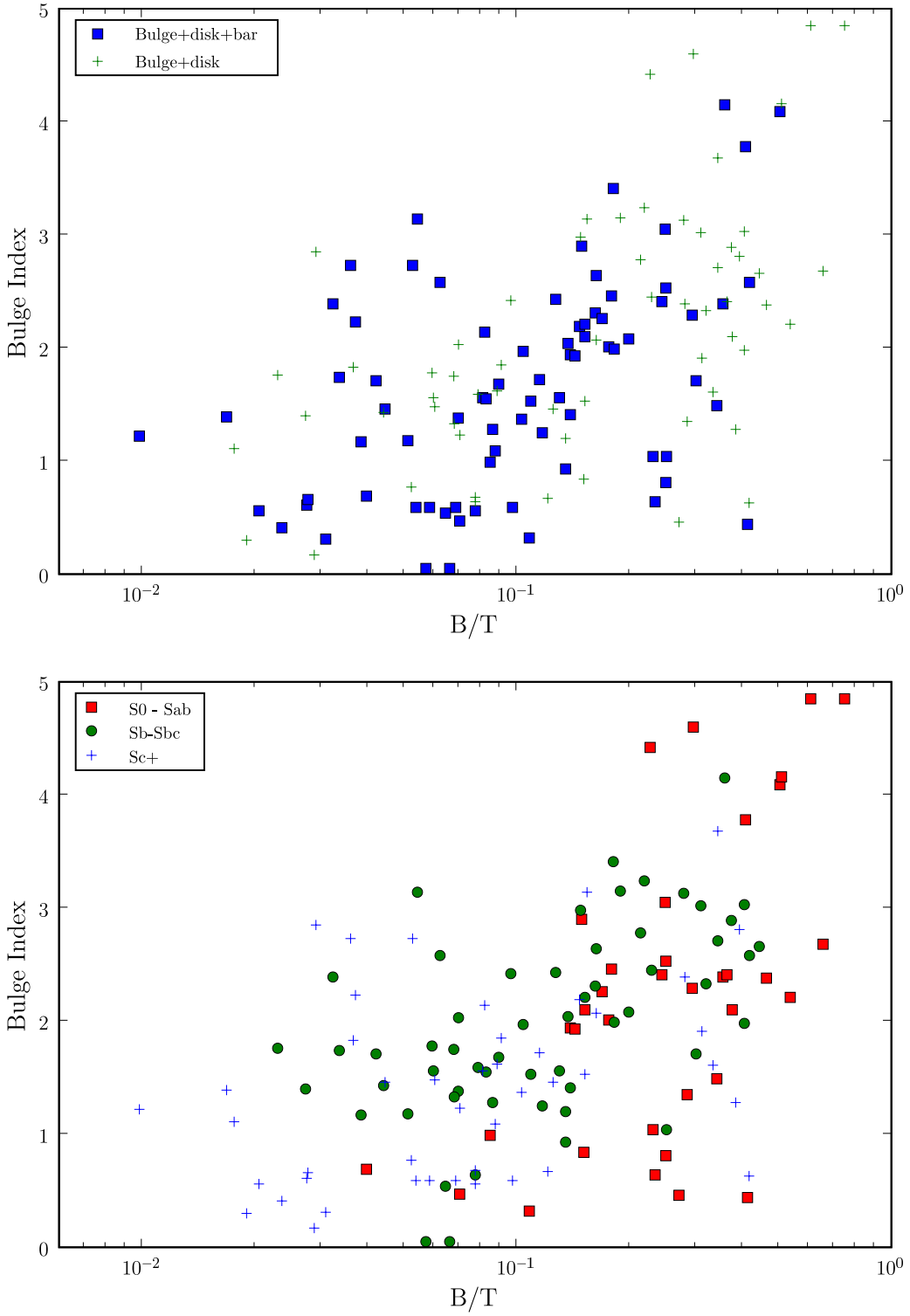

Fig. 16.— In the top panel, B/T and bulge index coded according to bar class. Barred and unbarred galaxies overlap and have a wide range of B/T and Sérsic indexes. In the bottom panel, the plot is recoded to distinguish early ($S0 \leq T \leq Sab$), intermediate ($Sb \leq T \leq Sbc$), and late ($T \geq Sc$) Hubble types. Bulges in early-type systems tend to have $B/T > 0.1$ and $n > 2$. Bulges in late type systems have $B/T < 0.1$ and $n < 2$. Intermediate Hubble types span the range of B/T and n between early and late types.

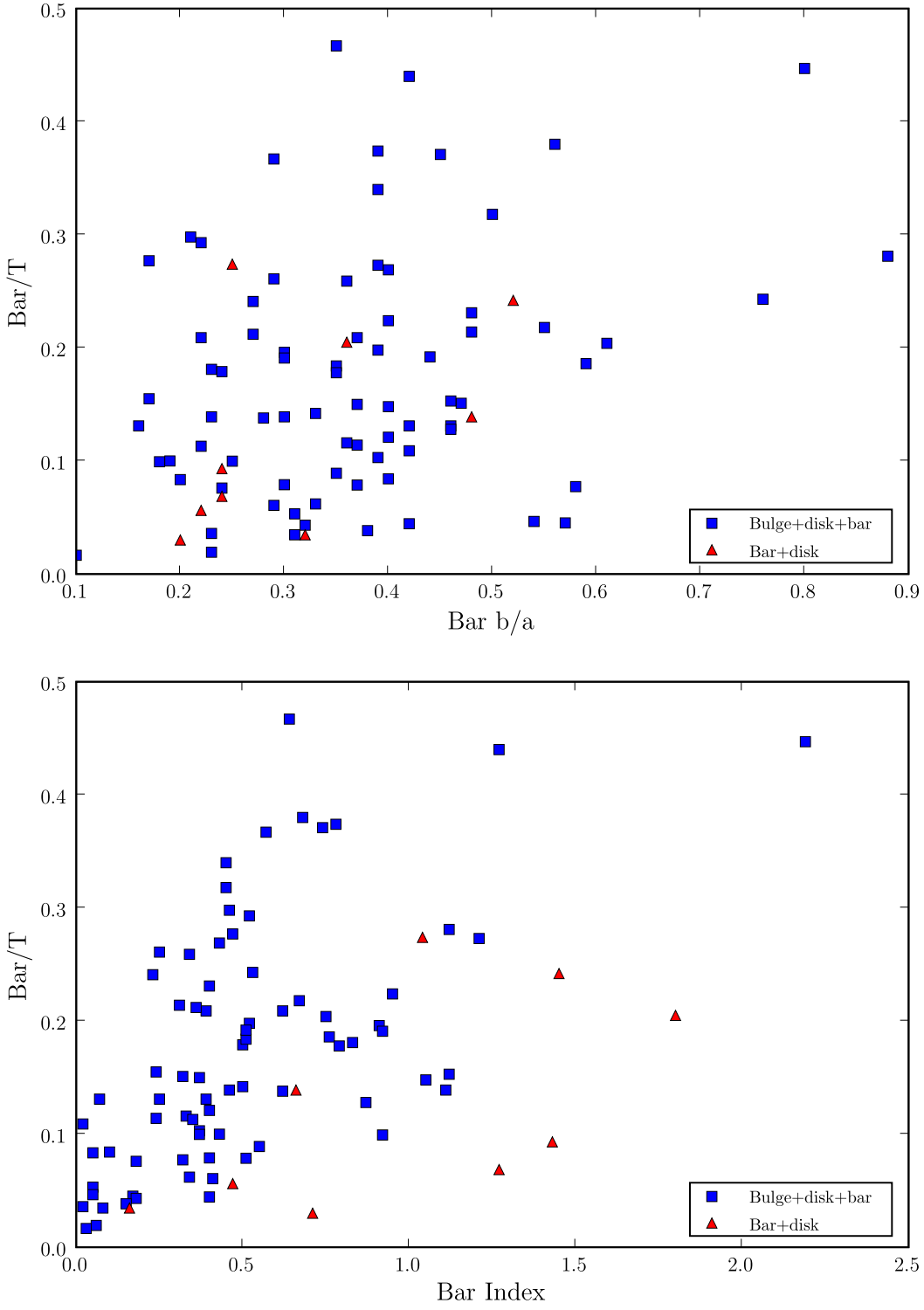

Fig. 17.— Bar/T is plotted against bar b/a and bar Sérsic index. Bar/T does not correlate well with b/a, but stronger (high Bar/T) bars tend to be more centrally concentrated.

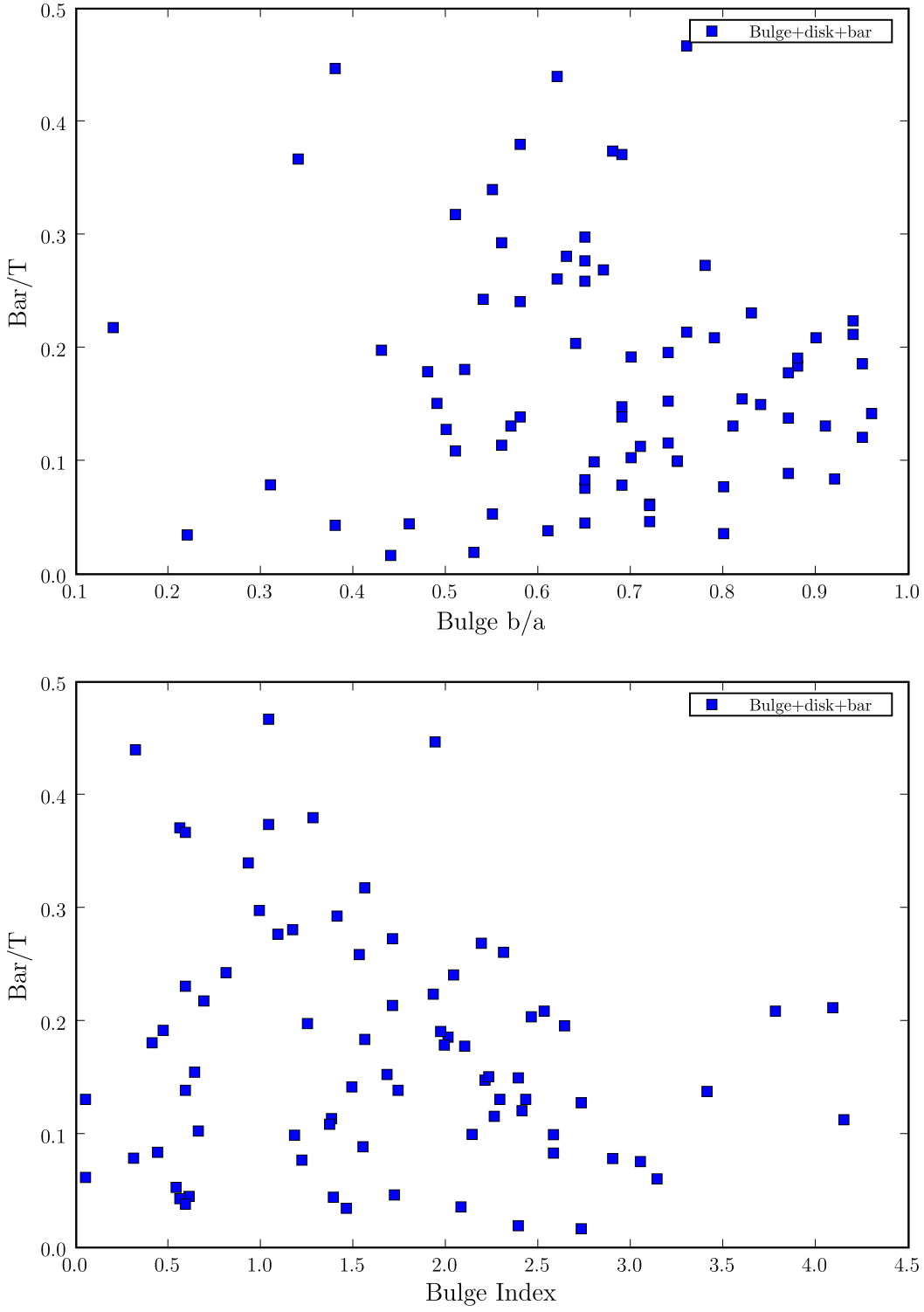

Fig. 18.— Bar/T is plotted against bulge b/a and bulge Sérsic index. Bar strength does not correlate with this these bulge parameters.

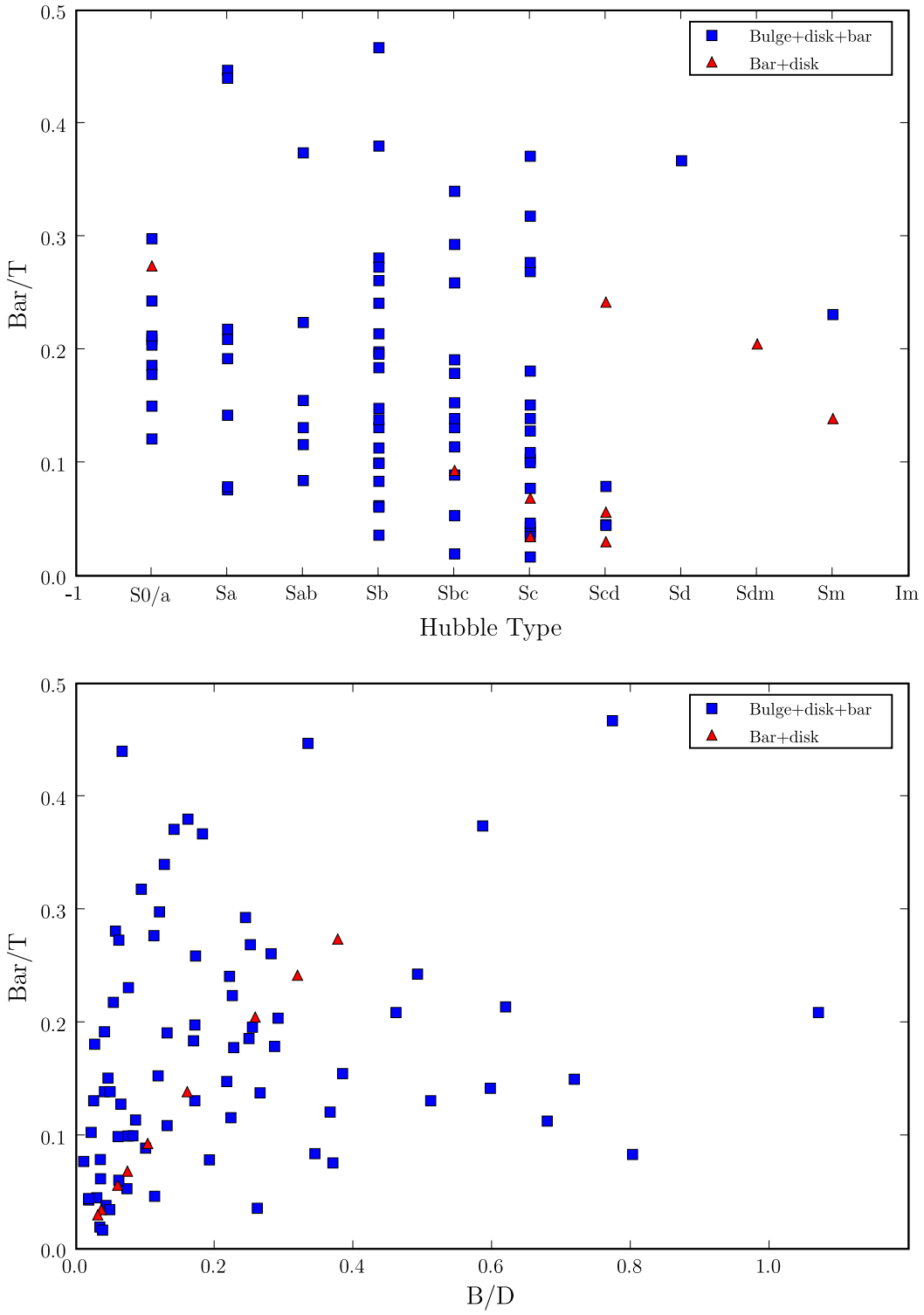

Fig. 19.— The distribution of Bar/T is plotted as a function of Hubble type and of B/D. Bar strength varies widely with both Hubble type and B/D.

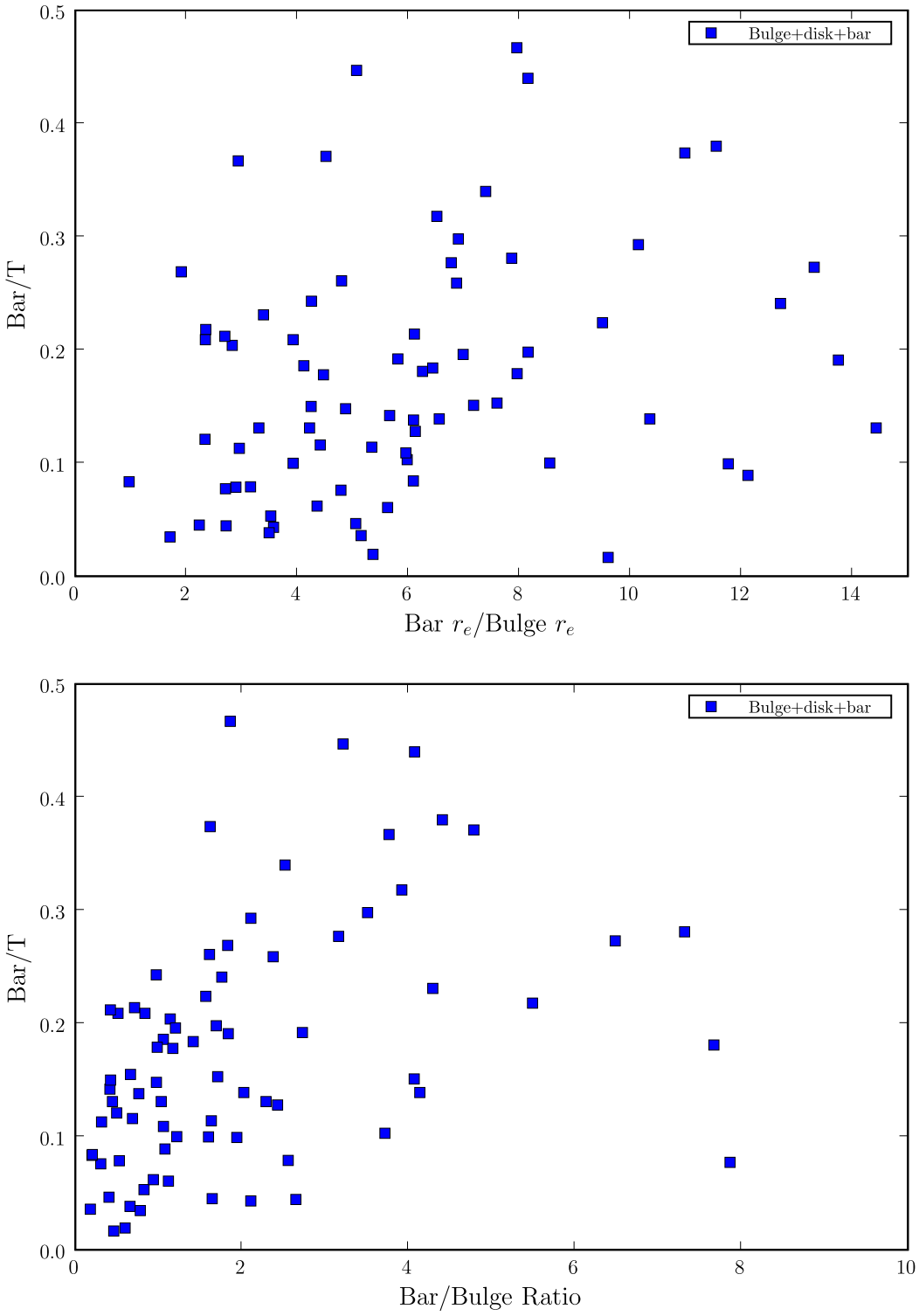

Fig. 20.— The top panel tests bar strength versus concentration of the bar with respect to the bulge. Bar/T tends to rise as the bar becomes more extended with respect to the bulge. The bottom panel plots bar/T versus $Bar/Bulge$ mass ratio. Bar/T becomes stronger as bar becomes more massive relative to the bulge.

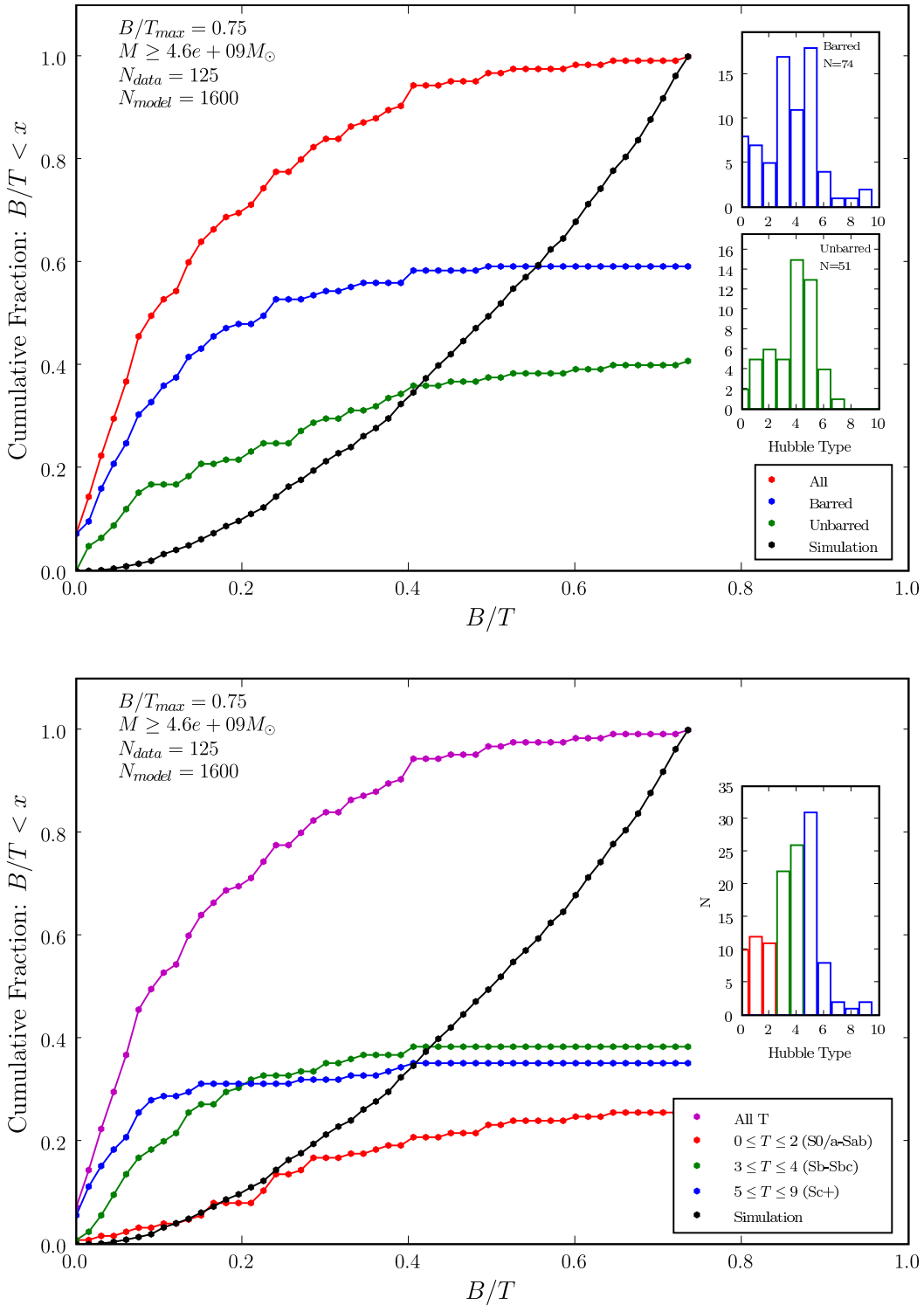

Fig. 21.— The top panel displays the cumulative fraction of B/T sorted by bar class. The bottom panel displays the distribution sorted by Hubble type. The black line results from LCDM-based simulations of galaxy formation. All simulated galaxies experienced at least one major merger of mass ratio 4:1 or lower. The lower mass limit is approximately the minimum stellar mass calculated for our sample.

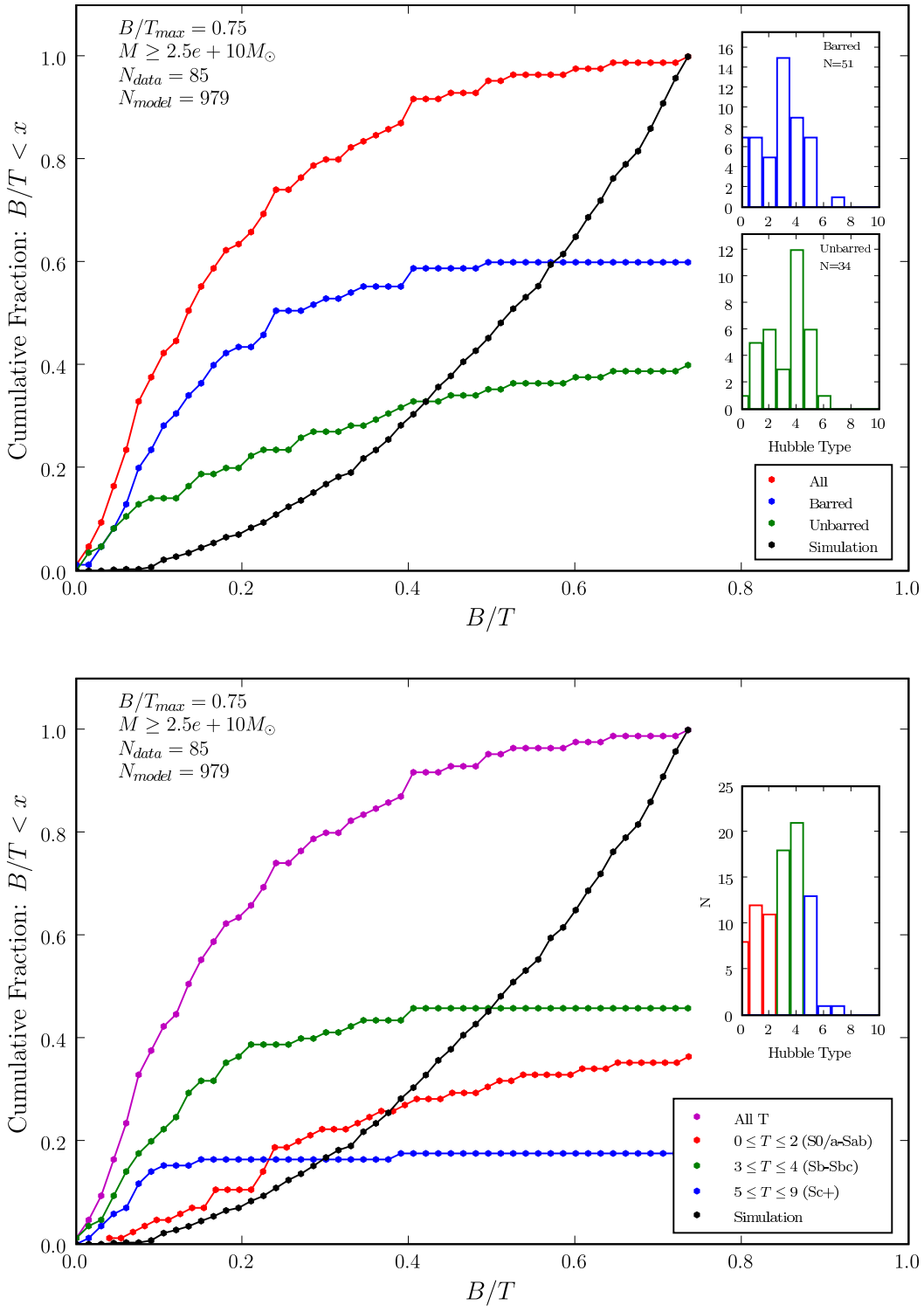

Fig. 22.— This is panel is identical to Figure 21 except that the lower mass limit has been increased to $2.5 \times 10^{10} M_{\odot}$.

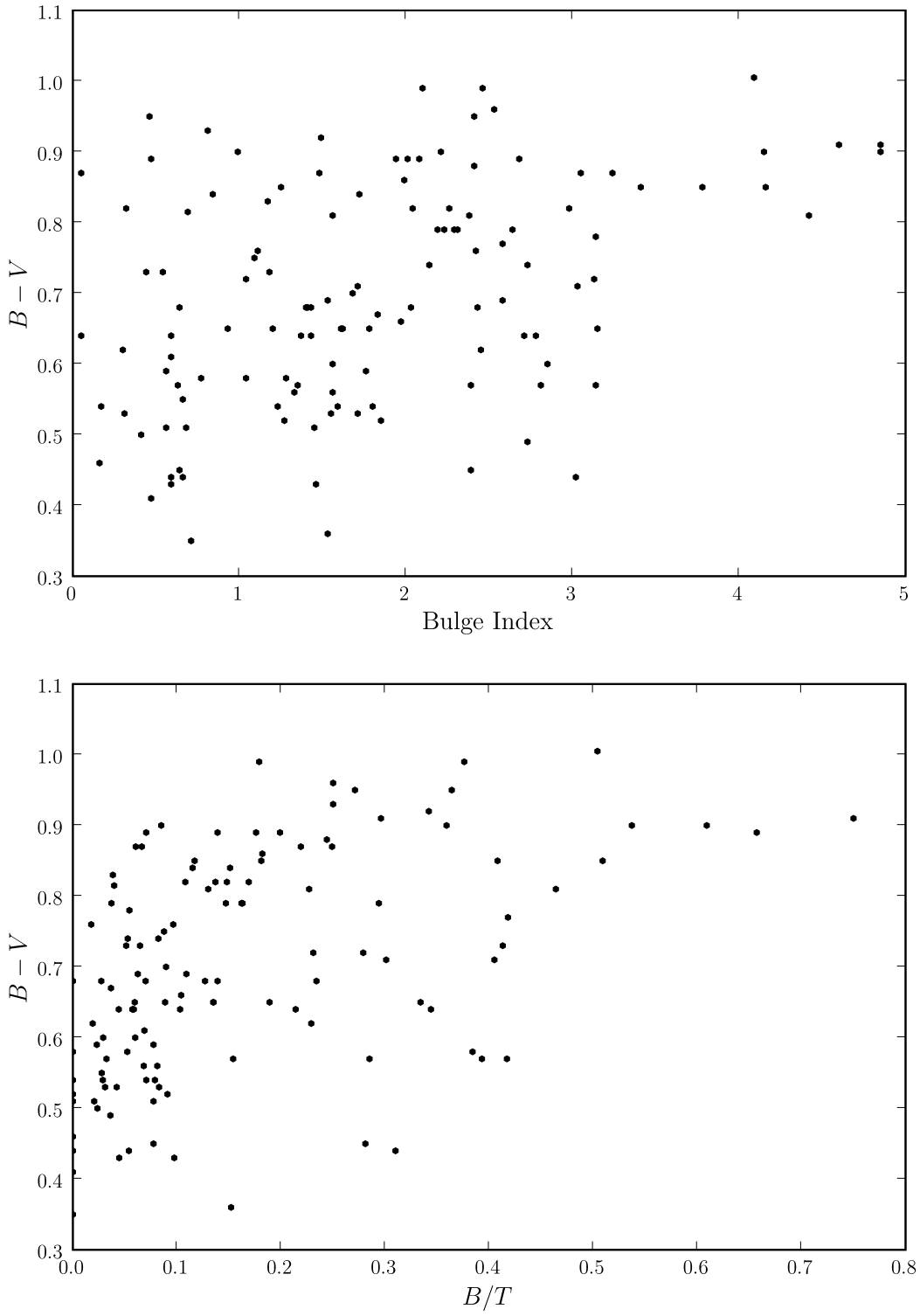

Fig. 23.— In the top panel, $B-V$ color is plotted against bulge Sérsic index. Though a wide degree of scatter exists, galaxies with the lowest bulge indexes have the bluest colors while galaxies with the highest indexes have the reddest colors. In the bottom panel, $B-V$ is plotted against B/T. Galaxies with $B/T < 0.1$ tend to have bluer colors than the most massive bulges. Many such systems have $B-V < 0.7$.

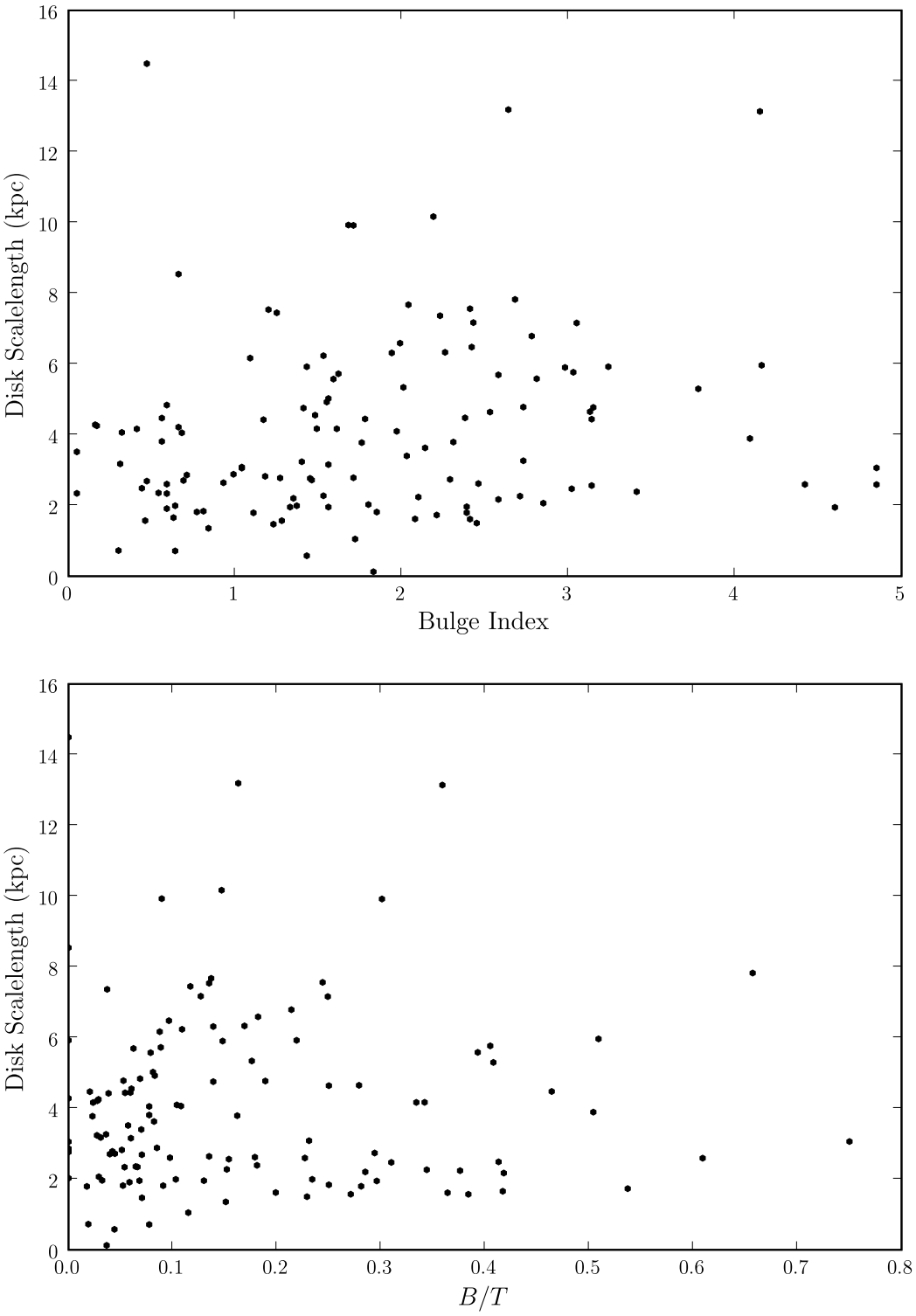

Fig. 24.— In the top panel, disk scalelength is plotted against bulge Sérsic index. Galaxies with $n < 2$ tend to have scalelengths < 5kpc, while for $n > 2$ the scalelengths are generally > 2kpc. The bottom panel shows disk scalelength versus B/T. For $B/T < 0.1$, scalelength is < 5kpc.

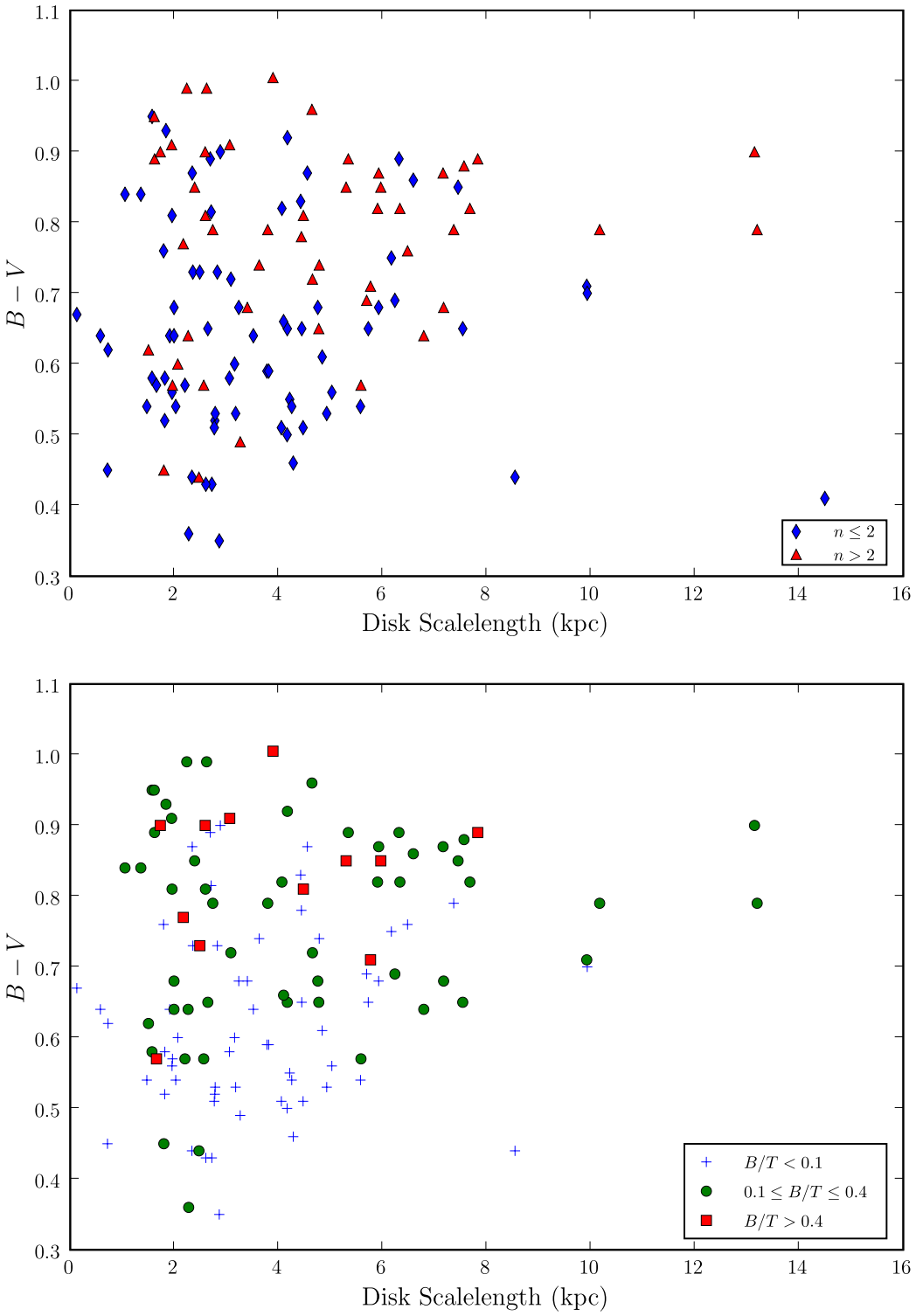

Fig. 25.— The top panel plots $B-V$ against disk scalelength; the points are color coded by bulge index. Galaxies with $n < 2$ tend to have scalelengths < 5kpc and $B-V < 0.7$. The bottom panel shows the same plot recoded according to B/T. A large fraction of systems with $B/T < 0.1$ have scalelengths < 5kpc and $B-V < 0.7$.

Table 1: Decomposition For NGC 4643

Fit		r_e or h ($''$)	r_e or h (kpc)	n	b/a	Position Angle	Fractional light
Stage 1	Sérsic	27.90	2.66	4.44	0.80	-51.03	100%
Stage 2	Bulge	23.86	2.30	4.16	0.80	-51.08	34.6%
	Disk	335.88	32.33	1.00	0.84	66.94	65.4%
Stage 3	Bulge	5.43	0.52	2.53	0.90	60.52	25.0%
	Disk	48.22	4.64	1.00	0.84	66.94	54.1%
	Bar	21.30	2.05	0.62	0.37	-45.84	20.9%

Table 2: Decomposition For NGC 4548

Fit		r_e or h ($''$)	r_e or h (kpc)	n	b/a	Position Angle	Fractional light
Stage 1	Sérsic	154.59	5.19	5.19	0.80	78.31	100%
Stage 2	Bulge	57.86	1.94	4.32	0.76	75.77	61.5%
	Disk	60.39	2.03	1.00	0.75	-32.54	38.5%
Stage 3	Bulge	6.98	0.23	1.56	0.88	-66.50	13.0%
	Disk	58.22	1.96	1.00	0.75	-32.54	68.6%
	Bar	44.91	1.51	0.51	0.35	66.65	18.4%

Table 3: Mass Breakdown of Galactic Structures

Structure	Mass (%)
Bulges	23.5
Disks	65.7
Bars	10.8
Classical bulges	15.5
Pseudobulges	4.7